Chapter 23

Local Mesh Free Methods in Linear Elasticity and Fracture Mechanics

Chapter details

Chapter DOI:

https://doi.org/10.4322/978-65-86503-83-8.c23

Chapter suggested citation / reference style:

Oliveira, Tiago, et al. (2022). "Local Mesh Free Methods in Linear Elasticity and Fracture Mechanics". *In* Jorge, Ariosto B., et al. (Eds.) *Fundamental Concepts and Models for the Direct Problem*, Vol. II, UnB, Brasilia, DF, Brazil, pp. 899–958. Book series in Discrete Models, Inverse Methods, & Uncertainty Modeling in Structural Integrity.

P.S.: DOI may be included at the end of citation, for completeness.

Book details

Book: Fundamental Concepts and Models for the Direct Problem

Edited by: Jorge, Ariosto B., Anflor, Carla T. M., Gomes, Guilherme F., & Carneiro, Sergio H. S.

Volume II of Book Series in:

Discrete Models, Inverse Methods, & Uncertainty Modeling in Structural Integrity

Published by: UnB City: Brasilia, DF, Brazil Year: 2022

DOI: https://doi.org/10.4322/978-65-86503-83-8

Local Mesh Free Methods in Linear Elasticity and Fracture Mechanics

Tiago Oliveira[1], Wilber Vélez[1] and Artur Portela[2*]

[1]Post-Graduate Program - Structural Engineering and Construction, University of Brasilia, Brazil. E-mail: tiago.antuney@gmail.com and wilbervelez@hotmail.com
[2]Post-Graduate Program - Structural Engineering and Construction, University of Brasilia, Brazil. E-mail: a3portela@gmail.com
*Corresponding author

Abstract

This chapter presents the most recent developments on mesh free numerical methods at the Department of Civil Engineering and Environment of the University of Brasília. Therefore, the concern of this chapter is a local mesh free method for solving linear elastic and fracture mechanics two-dimensional problems. For a nodal discretization of the problem domain, based in the work theorem from the theory of structures, the global system of equilibrium equations is constructed using a node-by-node process, performed in the local domain of each node. The reduced numerical integration is implemented to improves the model accuracy. Both regular and irregular nodal distributions can be considered, which makes it a reliable model. Local mesh free numerical methods depends on two arbitrary parameters for the analysis: the size of the compact support, which control the accuracy; and the local domain of integration, which control the efficiency. Both parameters are automatically defined by means of a multi-objective optimization process, based on genetic algorithms and symbiotic organism search algorithm, which makes it a robust model. Linear elastic fracture mechanics applications of local mesh free are performed through the singularity subtraction technique (SST), which regularizes the elastic field, before the numerical solution, thus introducing the stress intensity factors (SIF) as additional primary unknowns of the problem. Hence, the numerical model performs a direct computation of the SIF and does not require a refined discretization to obtain accurate results which, therefore, is an efficient model strategy. On all this cases, benchmark problems were solved for an assessment of the accuracy and efficiency of these techniques.

Keywords: Meshfree; Work theorem; Multi-objective optimization; Singularity Subtraction Technique.

1 Introduction

This section provides a brief overview on mesh free numerical methods over the recent years. Several widely used numerical methods are outlined in a concise manner and should be a good way to introduce the reader to those methods.

Mesh free, or meshless, have some advantages when compared to mesh-based methods, such as the Finite Element Method (FEM) and the Boundary Element Method (BEM), see Basu et al. [2003]. The essential feature of these methods is that they perform the discretization of the problem domain and boundaries with a set of scattered field nodes that do not require any mesh for the approximation of the field variables. In general, their formulation is based in the weighted-residual method, see Finalyson [1972].

Some of these meshless methods are based on a weighted-residual weak-form formulation. After discretization, the weak form is used to derive a system of algebraic equations through a process of numerical integration using sets of background cells, globally or locally constructed in the domain of the problem. Research on meshfree methods, based on a weighted-residual weak-form formulation, significantly increased after the publication of the Diffuse Element Method (DEM), introduced by Nayroles et al. [1992]. The Reproducing Kernel Particle Method (RKPM), presented by Liu et al. [1995], and the Element-free Galerkin (EFG) method, presented by Belytschko et al. [1994b], were the first weak-form meshless methods applied in solid mechanics.

All these weak-form meshless methods rely on background cells for the integration of the weighted-residual weak form over the global domain, in the process of the generation of the system of algebraic equations and therefore, they are not truly meshless methods.

In order to overcome the use of a global integration background mesh, a class of meshfree methods based on local weighted-residual weak forms, such as the Meshless Local Petrov–Galerkin (MLPG) method, presented by Atluri and Zhu [1998] and also by Atluri and Shen [2002]; the Meshless Local Boundary Integral Equation (MLBIE) method, presented by Zhu et al. [1998]; the Local Point Interpolation Method (LPIM), presented by Liu and Gu [2001], and the Local Radial Point Interpolation Method (LRPIM) presented by Liu et al. [2002], have been developed. Among them, the most popular of these methods is the MLPG, based on a moving least-squares (MLS) approximation. Later, the MLPG was implemented with the Finite Volume Method (FVM), as presented by Atluri et al. [2004], which improved the efficiency of the previous method.

The main difference of the MLPG method to other global meshless methods, such as EFG or RKPM, is that local weak forms are used for integration on overlapping regular-shaped local subdomains, instead of global weak forms and consequently the method does not require the use of a background global mesh, but only a background local grid which usually has a simple shape.

One of the issues faced by many numerical methods is solution instability when reduced integration is considered. In FEM, elements with a reduced integration are commonly employed because they are computationally efficient and avoid locking of fully integrated elements. But the main drawback is that these elements are susceptible to spurious singular modes, named as hourglass modes, which are zero-energy modes in which the element can deform without an associated increase of the internal energy. Stabilization techniques are usually employed to prevent these undesired effects, as presented by Zienkiewicz and Taylor [1983] and Bathe [2014].

This is also an issue faced by many mesh free methods, resulting in well known unstable hourglass deformation and zero-energy modes, such as the EFG, as reported by Beissel and Belytschko [1996], and the RKPM, as reported by Belytschko et al. [2000]. For local mesh free methods, the nodal integration was considered to improve computational efficiency, leading to unstable performance during the integration and formation of the stiffness matrix. Since each domain of integration is associated with just one integration point, which is the node, the integration of higher order functions inevitably causes fatal instabilities. In order to overcome these instabilities that are present in direct nodal integration, Taylor series expansions have been used, to serve as stabilization terms, as presented by Liu et al. [1985] for FEM, and by Liu et al. [1996] and Liu et al. [2007] for mesh free methods. While stable, the main problem of this stabilization technique is that it requires the computation of high order derivatives, nevertheless.

The mesh free discretization parameters, the compact support size and the local domain size,

are paramount and greatly affect the efficiency of a mesh free analysis. Most mesh free methods and author define both parameters arbitrarily depending on the nodal distribution, later studied by Moussaoui and Bouziane [2013] for the MLPG. Heuristically defined discretization parameters are not optimal and in most cases, inefficient.

Later, optimization attempts were carried out by Baradaran and Mahmoodabadi [2009] for two dimensional heat conduction problems, by Bagheri et al. [2011] for three dimensional elastostatic problems, and by Ebrahimnejad et al. [2015] for MLPG-FVM with adaptive refinement technique; all of them with Genectic Algorithm (GA). Even though successful, their attempts were time consuming and bounded to the analytical solution, which limits their usefulness.

In linear elastic fracture mechanics, the stress field becomes infinite at the crack tip, as presented by Brahtz [1933] and Williams [1952], becoming a source of singularity in numerical modeling. In order to overcome this difficulty, different ways have been used to model crack discontinuities.

In early attempts, Carpinteri et al. [2003] used the EFG considering a virtual extension of the crack in the tangent direction at the crack tip, meanwhile Wen and Aliabadi [2007] and Fleming et al. [1997] consider enriched basis/weight functions to mathematically capture jumps across crack displacement fields. More recently, Nguyen et al. [2020] used the mesh free particle method for thermal-mechanical crack growth analysis and Qingbo et al. [2021] used LRPIM to model shear crack propagation, both with enriched functions. The main drawback of this modeling strategy is that a limitation of the enrichment area must be considered in the presence of a densely distribution of cracks or crack tips too close to the boundaries. Different approaches were attempted to overcome this drawback. Rabczuk and Belytschko [2007] presented a method without the representation of the crack topology, Bordas et al. [2008] performed the analysis without near-tip enrichment, with extrinsic discontinuous enrichment; and Liu et al. [2004] presented a method with crack-tip specific enrichment functions used to simulate failure.

To avoid representing the singularity entirely, Symm [1963] subtracted the singularity from the numerical model, introducing the Singularity Subtraction Technique (SST). The method was used by Xanthis et al. [1981] to solve anti-plane problems and by Aliabadi et al. [1987] to solve crack problems with the Boundary Element Method (BEM).

2 Moving Least Square (MLS) Approximation

MLS approximation, schematically represented in Figure 1 for one-dimensional approximation,

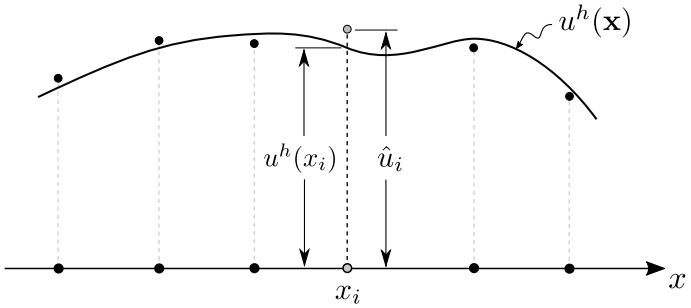

Figure 1: Schematic representation of the MLS approximation in one dimension.

is based on three components: a weight function of compact support associated with each node, a complete set of polynomial basis functions and a set of coefficients that are function of the space coordinates, as presented by Atluri and Zhu [1998]. In the following, the local mesh free method uses the basic MLS mesh-free terminology presented by Atluri and Zhu [2000].

Consider the domain of a body Ω with boundary Γ and let $N = \{\mathbf{x}_1, \mathbf{x}_2, ..., \mathbf{x}_N\} \in \Omega$ be a set of scattered nodal points that represents a mesh free discretization. It can be seen that some of them are located on the boundary Γ, as represented in Figure 2. The distribution of nodes in Ω and Γ is represented by $\mathbf{x}_i$, while Ω_s, represented as Ω_P, Ω_Q and Ω_R, is the local compact support of a node $\mathbf{x}_i$, represented as $\mathbf{x}_P$, $\mathbf{x}_Q$ and $\mathbf{x}_R$. $\Omega_{\mathbf{x}}$ is the domain of definition of a sampling point $\mathbf{x}$ and Ω_q is the local weak-form domain or quadrature domain of a node $\mathbf{x}_i$.

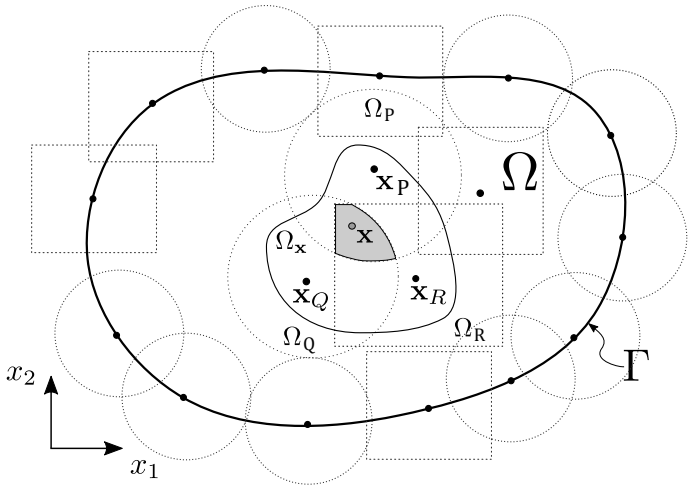

Figure 2: Representation of a meshless discretization of the domain.

Circular or rectangular local supports, centered at each nodal point, can be used. In a neighborhood of a sampling point $\mathbf{x}$, the domain of definition of MLS approximation is the subdomain $\Omega_{\mathbf{x}}$.

2.1 Shape Functions

Now, let $\Omega_{\mathbf{x}}$ be the MLS approximation domain of definition, in a neighborhood of a sampling point $\mathbf{x}$. To approximate the displacement $u(\mathbf{x}) \in \Omega_{\mathbf{x}}$, over a number of scattered nodes $\mathbf{x}_i \in \Omega$, $i = 1, 2, \ldots, n$, where the nodal parameters $\hat{u}_i$ are defined, the MLS approximation is given by

$$u^h(\mathbf{x}) = \mathbf{p}^T(\mathbf{x})\mathbf{a}(\mathbf{x}), \tag{1}$$

for $\mathbf{x} \in \Omega_{\mathbf{x}}$, in which

$$\mathbf{p}^T(\mathbf{x}) = [p_1(\mathbf{x}), p_2(\mathbf{x}), \ldots, p_m(\mathbf{x})], \tag{2}$$

is a vector of the complete monomial basis of order m and $\mathbf{a}(\mathbf{x})$ is the vector of unknown coefficients $a_j(\mathbf{x})$, $j = 1, 2, \ldots, m$ that are functions of the space coordinates $\mathbf{x} = [x_1, x_2]^T$, for two-dimensional problems.

The coefficient vector $\mathbf{a}(\mathbf{x})$ is determined by minimizing the weighted discrete L_2 norm

$$J(\mathbf{x}) = \frac{1}{2}\sum_{i=1}^{n} w_i(\mathbf{x}) \left[u^h(\mathbf{x_i}) - \hat{u}_i\right]^2 = \frac{1}{2}\sum_{i=1}^{n} w_i(\mathbf{x}) \left[\mathbf{p}^T(\mathbf{x}_i)\mathbf{a}(\mathbf{x}) - \hat{u}_i\right]^2, \tag{3}$$

with respect to each term of $\mathbf{a}(\mathbf{x})$, where $w_i(\mathbf{x})$ is the weight function associated with the node $\mathbf{x}_i$, with compact support that is $w_i(\mathbf{x}) > 0$, for all $\mathbf{x}$ in the support of $w_i(\mathbf{x})$. Figure 2 represents schematically the compact support of the MLS weight functions associated with a few scattered nodes. Finding the extremum of $J(\mathbf{x})$ with respect to each term of $\mathbf{a}(\mathbf{x})$, leads to

$$\mathbf{A}(\mathbf{x})\mathbf{a}(\mathbf{x}) = \mathbf{B}(\mathbf{x})\hat{\mathbf{u}}, \tag{4}$$

in which

$$\mathbf{A}(\mathbf{x}) = \sum_{i=1}^{n} w_i(\mathbf{x})\mathbf{p}(\mathbf{x}_i)\mathbf{p}^T(\mathbf{x}_i), \tag{5}$$

$$\mathbf{B}(\mathbf{x}) = [w_1(\mathbf{x})\mathbf{p}(\mathbf{x}_1), w_2(\mathbf{x})\mathbf{p}(\mathbf{x}_2), \ldots, w_n(\mathbf{x})\mathbf{p}(\mathbf{x}_n)] \tag{6}$$

and

$$\hat{\mathbf{u}} = [\hat{u}_1, \hat{u}_2, \ldots, \hat{u}_n]\,. \tag{7}$$

Solving equation (4) for $\mathbf{a}(\mathbf{x})$ yields

$$\mathbf{a}(\mathbf{x}) = \mathbf{A}^{-1}(\mathbf{x})\mathbf{B}(\mathbf{x})\hat{\mathbf{u}}, \tag{8}$$

provided $n \geq m$, for each sampling point $\mathbf{x}$, as a necessary condition for a well-defined MLS approximation. Finally, substituting for $\mathbf{a}(\mathbf{x})$ into equation (1) leads to the MLS approximation

$$u^h(\mathbf{x}) = \sum_{i=1}^{n} \phi_i(\mathbf{x})\hat{u}_i, \tag{9}$$

in which

$$\phi_i(\mathbf{x}) = \sum_{j=1}^{m} p_j(\mathbf{x}) \left[\mathbf{A}^{-1}(\mathbf{x})\mathbf{B}(\mathbf{x})\right]_{ji} \tag{10}$$

is the shape function of the MLS approximation corresponding to the node $\mathbf{x}_i$, schematically represented in Figure 3.

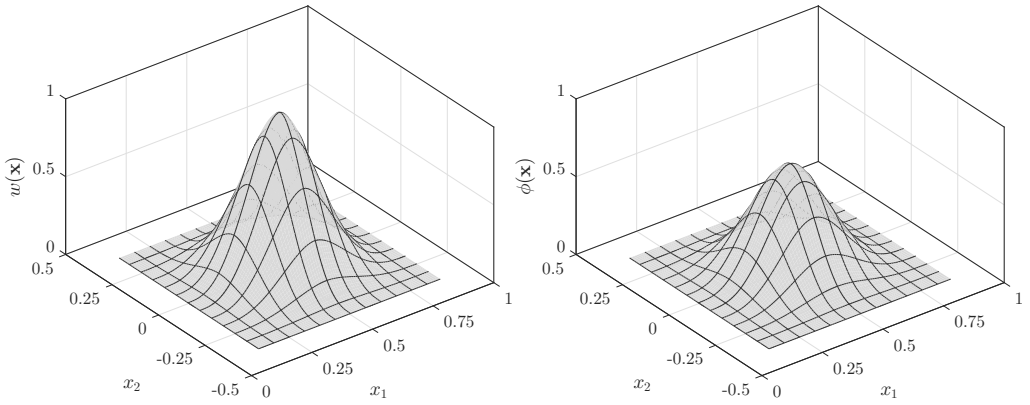

(a) Weight function (b) Shape function

Figure 3: Typical weight function and shape function of the MLS approximation for a node at $\mathbf{x} = [\mathbf{1/2} \quad \mathbf{0}]^{\mathbf{T}}$.

The MLS shape functions are not nodal interpolants that is $\phi_i(\mathbf{x}_j) \neq \delta_{ij}$. Since $\phi_i(\mathbf{x})$ vanishes for $\mathbf{x}$ not in the local domain of the node $\mathbf{x}_i$, the local character of the MLS approximation is preserved. The nodal shape function is complete up to the order of the basis. The smoothness of the nodal shape function is determined by the smoothness of the basis and of the weight function. The spatial derivatives of the shape function $\phi_i(\mathbf{x})$ are given by

$$\phi_{i,k} = \sum_{j=1}^{m} \left[p_{j,k}(\mathbf{A}^{-1}\mathbf{B})_{ji} + p_j(\mathbf{A}^{-1}\mathbf{B}_{,k} - \mathbf{A}^{-1}\mathbf{A}_{,k}\,\mathbf{A}^{-1}\mathbf{B})_{ji}\right], \tag{11}$$

in which $()_{,k} = \partial()/\partial x_k$.

2.2 Weight Functions

Weight functions $w_i(\mathbf{x})$, schematically represented in Figure 3, introduced in equation (3) for each node $\mathbf{x}_i$, have a compact support which defines the subdomain where $w_i(\mathbf{x}) > 0$, for all $\mathbf{x}$. For the sake of simplicity, this chapter considers rectangular compact supports with weight functions defined as

$$w_i(\mathbf{x}) = w_{i_x}(\mathbf{x})\, w_{i_y}(\mathbf{x}) \tag{12}$$

with the weight function given by the quartic spline function

$$w_{i_x}(\mathbf{x}) = \begin{cases} 1 - 6\left(\dfrac{d_{i_x}}{r_{i_x}}\right)^2 + 8\left(\dfrac{d_{i_x}}{r_{i_x}}\right)^3 - 3\left(\dfrac{d_{i_x}}{r_{i_x}}\right)^4 & \text{for } 0 \le d_{i_x} \le r_{i_x} \\ 0 & \text{for } d_{i_x} > r_{i_x} \end{cases} \tag{13}$$

and

$$w_{i_y}(\mathbf{x}) = \begin{cases} 1 - 6\left(\dfrac{d_{i_y}}{r_{i_y}}\right)^2 + 8\left(\dfrac{d_{i_y}}{r_{i_y}}\right)^3 - 3\left(\dfrac{d_{i_y}}{r_{i_y}}\right)^4 & \text{for } 0 \le d_{i_y} \le r_{i_y} \\ 0 & \text{for } d_{i_y} > r_{i_y}, \end{cases} \tag{14}$$

in which $d_{i_x} = \|x - x_i\|$ and $d_{i_y} = \|y - y_i\|$. The parameters r_{i_x} and r_{i_y} represent the size of the support for the node i, respectively in the x and y directions.

3 Structural Modeling

Consider the domain Ω of a body with boundary Γ, further divided in Γ_u and Γ_t, with $\Gamma = \Gamma_u \cup \Gamma_t$, as Figure 4 represents. The work theorem is defined in an arbitrary domain $\Omega_Q \in \Omega \cup \Gamma$, assigned to a reference point $Q \in \Omega_Q$, with boundary $\Gamma_Q = \Gamma_{Qi} \cup \Gamma_{Qt} \cup \Gamma_{Qu}$, in which Γ_{Qi} is the interior local boundary, and Γ_{Qt} and Γ_{Qu} are local boundaries that share the global boundaries, respectively the static boundary Γ_t and the kinematic boundary Γ_u; points P and R, have arbitrary local domains, respectively Ω_P and Ω_R.

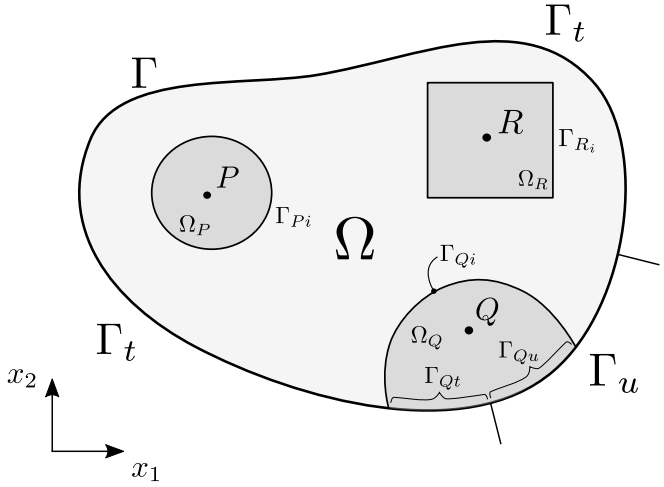

Figure 4: Representation of the body's domain Ω, with boundary Γ.

The mixed fundamental boundary value problem of linear elastostatics aims to find, in Ω, the distribution of stresses $\boldsymbol{\sigma}$, strains $\boldsymbol{\varepsilon}$ and displacements $\mathbf{u}$, when it has displacements $\overline{\mathbf{u}}$, constrained

on Γ_u, and is under the action of an external system of distributed surface and body forces with densities represented, respectively by $\bar{\mathbf{t}}$, on Γ_t and $\mathbf{b}$, in Ω.

The solution of the posed problem is a totally admissible elastic field that simultaneously satisfies the kinematic admissibility and the static admissibility. If this solution exists, see Fichera [2006], it can be shown that it is unique, provided linearity and stability of the material are admitted. Such is the uniqueness theorem of Kirchhoff [1859] which, in the framework of the variational calculus, leads to the theorem of virtual displacements and the theorem of virtual stresses. Since these theorems consider the totally admissible elastic field that is the actual solution of the posed problem, they are only particular cases of the general work theorem. Therefore, the general work theorem will be used to solve the posed problem.

Now consider the domain Ω of a body, loaded by a system of external forces under the conditions already mentioned, and a statically admissible stress field $\boldsymbol{\sigma}$, which therefore satisfies

$$\mathbf{L}^T\boldsymbol{\sigma} + \mathbf{b} = \mathbf{0}, \tag{15}$$

in Ω, with boundary conditions

$$\mathbf{t} = \mathbf{n}\,\boldsymbol{\sigma} = \bar{\mathbf{t}}, \tag{16}$$

specified on Γ_t; where $\mathbf{L}$ is a matrix differential operator; $\mathbf{t}$ denotes traction components; $\bar{\mathbf{t}}$ denotes prescribed tractions and $\mathbf{n}$ is the matrix of the components of the unit normal to the boundary outwardly directed.

In the body, consider an arbitrary local domain $\Omega_Q \in \Omega \cup \Gamma$, assigned to a reference point $Q \in \Omega_Q$, with boundary $\Gamma_Q = \Gamma_{Qi} \cup \Gamma_{Qt} \cup \Gamma_{Qu}$, in which Γ_{Qi} is the interior local boundary, with local boundaries Γ_{Qt} and Γ_{Qu} sharing the global boundaries, respectively the static boundary Γ_t and the kinematic boundary Γ_u, as Figure 4 clearly represents. The work theorem will be derived for this arbitrary local domain Ω_Q. This local domain $\Omega_Q \cup \Gamma_Q \in \Omega \cup \Gamma$ can be overlapping with other similar sub-domains that can be defined in the body, due to its arbitrariness.

3.1 The Work Theorem

The work theorem establishes an energy relationship, in an arbitrary local domain $\Omega_Q \in \Omega$, between two independent elastic fields that can be defined in the body. These elastic fields are, respectively, a statically admissible stress field $\boldsymbol{\sigma}$ that satisfies equilibrium with a system of external forces, and a kinematically admissible strain field $\boldsymbol{\varepsilon}^*$ that satisfies compatibility with a set of constrained displacements. Expressed as an integral form, defined in the domain $\Omega_Q \cup \Gamma_Q$, the work theorem can be written in a compact way, simply as

$$\int_{\Gamma_Q} \mathbf{t}^T\mathbf{u}^*\,\mathrm{d}\Gamma + \int_{\Omega_Q} \mathbf{b}^T\mathbf{u}^*\,\mathrm{d}\Omega = \int_{\Omega_Q} \boldsymbol{\sigma}^T\boldsymbol{\varepsilon}^*\,\mathrm{d}\Omega, \tag{17}$$

in which no constitutive relation links the stress $\boldsymbol{\sigma}$ and the strain $\boldsymbol{\varepsilon}^*$. Therefore, they do not depend on each other, as Figure 5 schematically represents, where Dbc and Tbc stands for Displacement boundary condition and Traction boundary condition, respectively.

The statically admissible stress field $\boldsymbol{\sigma}$, can be any field that guarantee the equilibrium with the system of external forces, therefore satisfying equations (15) and (16). This elastic field is not necessarily the stress that the system of external forces actually introduces in the body.

The kinematically admissible strain field $\boldsymbol{\varepsilon}^*$, can be any field, assuming continuous displacements $\mathbf{u}^*$ with small derivatives, compatible with an arbitrary set of constraints specified on the kinematic boundary. This elastic field is not necessarily the strain that actually settled in the body.

Lastly, the local domain $\Omega_Q \cup \Gamma_Q$ is an arbitrary sub-domain of the body, associated with the reference point Q, as represented in Figure 4, where the independent fields $\boldsymbol{\sigma}$ and $\boldsymbol{\varepsilon}^*$ are established.

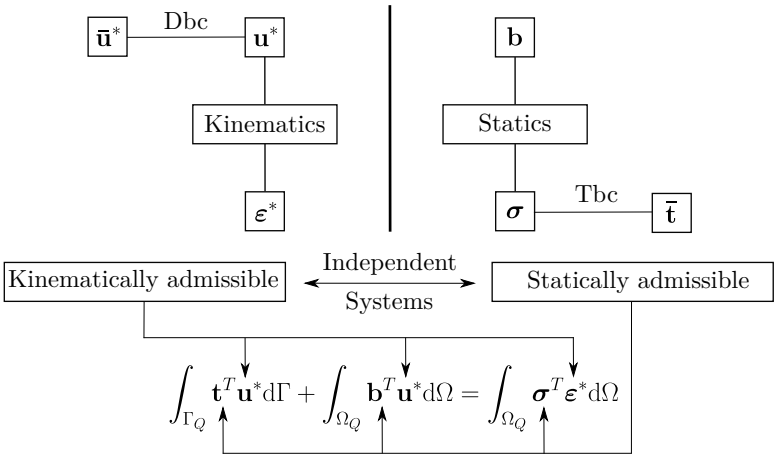

Figure 5: Schematic representation of the work theorem, an energy relationship, valid in an arbitrary local domain $\Omega_\mathbf{Q} \cup \Gamma_\mathbf{Q} \in \Omega$, between two independent fields.

3.2 Kinematic Formulation

Different formulations of local mesh free methods can be derived when one of the two independent fields are locally defined in the body, usually in accordance with some particular convenience of the numerical method formulation.

Kinematic formulations consider a particular specification of the strain field $\boldsymbol{\varepsilon}^*$, leading thus to a mechanical equilibrium equation, which is used in numerical model to generate the respective stiffness matrix. A simple case of a kinematic formulation, based on a strain field generated by a rigid-body displacement, is therefore presented.

3.3 Rigid-Body Displacement Formulation

One of the key feature of the work theorem, the complete independence of the admissible fields $\boldsymbol{\sigma}$ and $\boldsymbol{\varepsilon}^*$, allow the formulation to be simplified by defining kinematically admissible strain fields. Hence, the simplest and obvious choice is to use a strain field generated by a rigid-body displacement that can be defined as

$$\mathbf{u}^*(\mathbf{x}) = \mathbf{c}, \tag{18}$$

in which $\mathbf{c}$ is a constant vector that conveniently generates null strains

$$\boldsymbol{\varepsilon}^*(\mathbf{x}) = \mathbf{0}. \tag{19}$$

The great virtue of this formulation is the simplicity used in the generation of the strain field. Additionally, this formulation leads to a simple form of equilibrium equations that, in the absence of body forces, involves only non-singular boundary integrals with no domain terms.

When the rigid-body displacement formulation is considered, the work theorem, equation (17), simply leads to the equation

$$\int_{\Gamma_Q - \Gamma_{Qt}} \mathbf{t}\,\mathrm{d}\Gamma + \int_{\Gamma_{Qt}} \bar{\mathbf{t}}\,\mathrm{d}\Gamma + \int_{\Omega_Q} \mathbf{b}\,\mathrm{d}\Omega = \mathbf{0} \tag{20}$$

which is nothing else other than the local version of Euler-Cauchy stress principle that is sometimes referred to as the defining principle of continuum mechanics. Equation (20) presents the mechanical equilibrium of tractions and body forces, in the domain Ω_Q, in an integral form. Therefore, it is used to generate the stiffness matrix associated to the local node.

4 Numerical Modeling Strategy

Based on the work theorem and choosing a proper and convenient kinematic formulation, the numerical model can derive the equilibrium equations that are used to generate the stiffness matrix. This numerical modeling strategy is adopted to solve the actual elastic problem set up in Section 3.

First of all, locally defined in the work theorem, an appropriate strain field $\boldsymbol{\varepsilon}^*$ is specified in the kinematic formulation. The mesh free numerical model considers the arbitrary rigid-body displacement, presented in Section 3.2, thus leading to the equilibrium equation (20).

On the other hand, the statically-admissible local field $\boldsymbol{\sigma}$, will be always assumed as the elastic field that actually settles in the body, required to satisfy equilibrium with a system of external forces and loaded by the actual system of distributed surface and body forces, with the actual displacement constraints.

Besides satisfying static admissibility, through equations (15) and (16), , or through equation (20), this elastic field also satisfies kinematic admissibility defined as

$$\boldsymbol{\varepsilon} = \mathbf{L}\,\mathbf{u}, \tag{21}$$

in Ω, with boundary conditions

$$\mathbf{u} = \overline{\mathbf{u}}, \tag{22}$$

on Γ_u, in which continuous displacements are assumed with small derivatives, leading to geometrical linearity of the strain field, in order to satisfy compatibility. Therefore, equations (22), which specifies the constraints of the actual displacements, must be enforced in the numerical model, in order to provide a unique solution of the posed problem.

5 Local Mesh free Method

The discretization of the domain is performed considering a set of scattered nodes in the domain Ω and boundary $\Gamma = \Gamma_u \cup \Gamma_t$. Each node of the mesh free discretization is associated with its local domain, as schematically represented in Figure 6, where the reference nodes P, Q and R can be seen. These nodes have associated local domains Ω_P, Ω_Q and Ω_R; the local domain Ω_Q, assigned to the node Q, where the work theorem is defined, has boundary $\Gamma_Q = \Gamma_{Qi} \cup \Gamma_{Qt} \cup \Gamma_{Qu}$, in which Γ_{Qi} is the interior local boundary and $\Gamma_{Qt} \in \Gamma_t$ and $\Gamma_{Qu} \in \Gamma_u$.

In general, this local domain is a circular or rectangular region and centered at the respective node, for the sake o simplicity, where the rigid-body displacement formulation of the work theorem is defined as a local form of mechanical equilibrium. This local domain can assume any geometry and is highly susceptible to optimization and topology studies.

The MLS approximation uphold the local aspect of the formulation,throughout the compact support of each node, where the respective MLS shape functions are defined. As presented in Section 2, local compact supports can also have circular or rectangular shapes, centered at each node. The size of the compact support determines, in a neighborhood of a sampling point, the respective MLS domain of definition of this reference point, as schematically represented in Figure 2.

The domain of definition contains all the nodes that do not vanish, within a compact support at a sampling point, when constructing the MLS shape functions. Therefore, the union of the MLS domains of definition of all points in the local domain of each node, defines the domain of influence

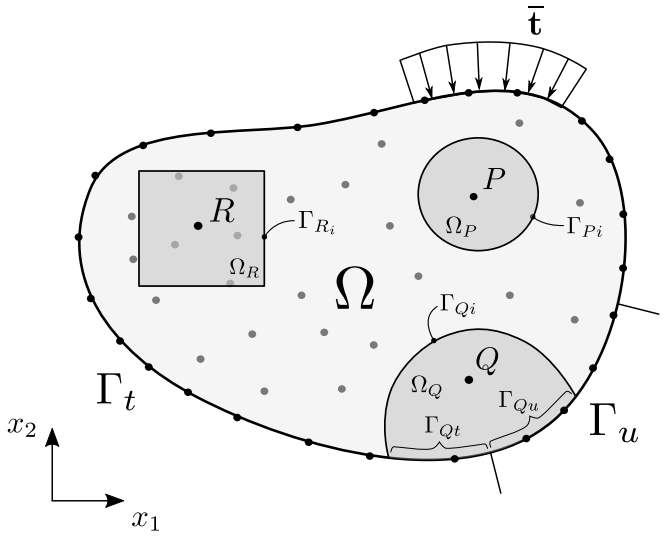

Figure 6: Mesh free discretization of the domain Ω and boundary $\Gamma = \Gamma_{\mathbf{u}} \cup \Gamma_{\mathbf{t}}$.

of the node. Based on this domain of influence of each node, the local mesh free method perform a node-by-node stiffness computation to generate the respective rows of the global stiffness matrix of the node.

The rigid-body displacement mesh free formulation of the local work theorem, equation (20), can be written, in the absence of body forces, simply as

$$\int\limits_{\Gamma_Q - \Gamma_{Qt}} \mathbf{t}\, \mathrm{d}\Gamma = -\int\limits_{\Gamma_{Qt}} \overline{\mathbf{t}}\, \mathrm{d}\Gamma \tag{23}$$

which is nothing else than the mechanical equilibrium of the boundary tractions in the local domain Ω_Q.

Local mesh free numerical methods can be effectively formulated through a reduced integration of the equilibrium equation (23). For simplicity sake, linear variation of tractions is assumed on each boundary of the local domain, leading to a point-wise discrete form.

The reduced integration presented readily overcomes the well-known difficulties posed by the reduced integration on mesh-based methods, regarding accuracy and stability of the solution, which makes the local mesh free formulation a reliable and robust method.

Therefore, for a linear variation of tractions, along each boundary segment of the local domain, the local form of equilibrium (23), can be accurately evaluated with only one quadrature point, centered on each segment, thus leading to

$$\frac{L_i}{n_i} \sum_{j=1}^{n_i} \mathbf{t}_{\mathbf{x}_j} = -\frac{L_t}{n_t} \sum_{k=1}^{n_t} \overline{\mathbf{t}}_{\mathbf{x}_k}, \tag{24}$$

in which n_i and n_t denote the total number of integration/quadrature points, or linear segments, defined on, respectively the interior local boundary $\Gamma_{Qi} = \Gamma_Q - \Gamma_{Qt} - \Gamma_{Qu}$, with length L_i, and the local boundary Γ_{Qt}, with length L_t. This equation effectively represents a point-wise discrete form of mechanical equilibrium of boundary tractions, evaluated at a set of points of the local domain Ω_Q.

For any given nodal distribution of scattered nodes, the local mesh free method with linear reduced integration, symbolically referred from now on as ILMF, an simple acronym that stands

for Integrated Local Mesh Free method, is used to compute the stiffness matrix. ILMF uses a node-by-node process to construct the stiffness matrix, throughout traction evaluation at each central point of boundary segments, by using equation (24) assigned to each node.

These local domains can assume rectangular or circular geometries, as schematically represented in Figure 7 for interior nodes, Figure 8 for corner nodes and Figure 9 for boundary nodes.

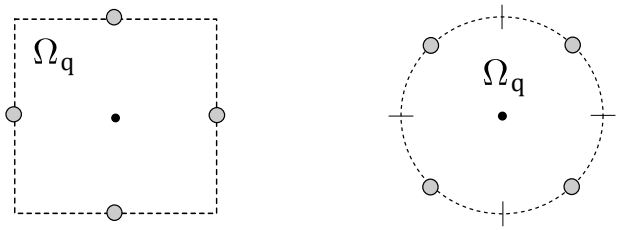

(a) Rectangular (b) Circular

Figure 7: Schematic representation of rectangular and circular local domains, with 1 integration point per side, or quadrant, of the local domain, for the computation of the local form (24) of ILMF.

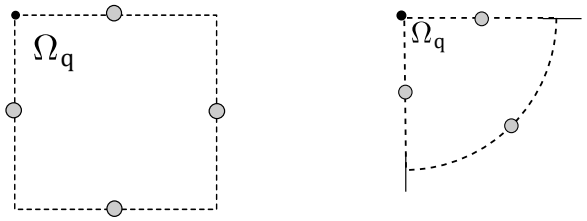

(a) Rectangular (b) Circular

Figure 8: Schematic representation of rectangular and circular local domains on corner nodes, with 1 integration point per side, or quadrant, of the local domain.

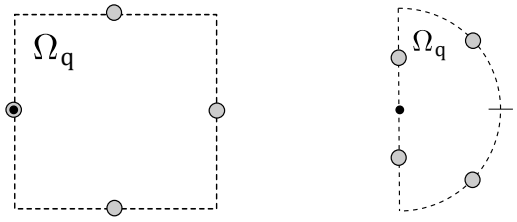

(a) Rectangular (b) Circular

Figure 9: Schematic representation of rectangular and circular local domains on boundary nodes, with 1 integration point per side, or quadrant, of the local domain. The integration point and the node share the same coordinates on one of the boundaries.

As ti can be seen, any special treatment for traction evaluation is considered in the linear reduced integration process.

The MLS approximation of a displacement component $u^h(\mathbf{x})$, is performed in terms of the unknown nodal parameters $\hat{u}_i$. Consequently, the approximation of the elastic field is also performed

in terms of the unknown nodal parameters $\hat{\mathbf{u}}$, as

$$\mathbf{u} = \begin{bmatrix} u^h(\mathbf{x}) \\ v^h(\mathbf{x}) \end{bmatrix} = \begin{bmatrix} \phi_1(\mathbf{x}) & 0 & \dots & \phi_n(\mathbf{x}) & 0 \\ 0 & \phi_1(\mathbf{x}) & \dots & 0 & \phi_n(\mathbf{x}) \end{bmatrix} \begin{bmatrix} \hat{u}_1 \\ \hat{v}_1 \\ \vdots \\ \hat{u}_n \\ \hat{v}_n \end{bmatrix} = \mathbf{\Phi}\,\hat{\mathbf{u}} \tag{25}$$

and

$$\boldsymbol{\varepsilon} = \mathbf{L}\,\mathbf{u} = \mathbf{L}\,\mathbf{\Phi}\,\hat{\mathbf{u}} = \mathbf{B}\,\hat{\mathbf{u}}, \tag{26}$$

in which geometrical linearity is assumed in the differential operator $\mathbf{L}$ and thus,

$$\mathbf{B} = \begin{bmatrix} \phi_{1,1} & 0 & \dots & \phi_{n,1} & 0 \\ 0 & \phi_{1,2} & \dots & 0 & \phi_{n,2} \\ \phi_{1,2} & \phi_{1,1} & \dots & \phi_{n,2} & \phi_{n,1} \end{bmatrix}. \tag{27}$$

Stress and traction components are respectively approximated as

$$\boldsymbol{\sigma} = \mathbf{D}\,\boldsymbol{\varepsilon} = \mathbf{D}\,\mathbf{B}\,\hat{\mathbf{u}} \tag{28}$$

and

$$\mathbf{t} = \mathbf{n}\,\boldsymbol{\sigma} = \mathbf{n}\,\mathbf{D}\,\mathbf{B}\,\hat{\mathbf{u}}, \tag{29}$$

in which $\mathbf{D}$ is the matrix of the elastic constants and $\mathbf{n}$ is the matrix of the components of the unit outward normal, defined as

$$\mathbf{n} = \begin{bmatrix} n_1 & 0 & n_2 \\ 0 & n_2 & n_1 \end{bmatrix}. \tag{30}$$

Accordingly, the MLS approximation of the integrated local form (24) is carried out in terms of the unknown nodal parameters $\hat{\mathbf{u}}$. Hence, this process leads to the system of two algebraic equations

$$\frac{L_i}{n_i} \sum_{j=1}^{n_i} \mathbf{n}_{\mathbf{x}_j} \mathbf{D} \mathbf{B}_{\mathbf{x}_j}\,\hat{\mathbf{u}} = -\frac{L_t}{n_t} \sum_{k=1}^{n_t} \bar{\mathbf{t}}_{\mathbf{x}_k} \tag{31}$$

that can be written as

$$\mathbf{K}_Q\,\hat{\mathbf{u}} = \mathbf{F}_Q, \tag{32}$$

in which $\mathbf{K}_Q$, denotes the stiffness matrix of the node Q, which is of the order $2 \times 2n$, where n represents the number of nodes of the influence domain of Q, given by

$$\mathbf{K}_Q = \frac{L_i}{n_i} \sum_{j=1}^{n_i} \mathbf{n}_{\mathbf{x}_j} \mathbf{D} \mathbf{B}_{\mathbf{x}_j} \tag{33}$$

and $\mathbf{F}_Q$ denotes the vector of forces

$$\mathbf{F}_Q = -\frac{L_t}{n_t} \sum_{k=1}^{n_t} \bar{\mathbf{t}}_{\mathbf{x}_k}. \tag{34}$$

For a numerical model with N nodes in total, in which M is the number of interior and static-boundary nodes, the assembly of equations (32) for all M nodes leads to the $2M \times 2N$ system of equations

$$\mathbf{K}\,\hat{\mathbf{u}} = \mathbf{F}. \tag{35}$$

Finally, the $N - M$ kinematic-boundary nodes, are used to generate the remaining equations of the problem. For each of these nodes, the kinematic boundary condition is imposed through a direct interpolation method as

$$\mathbf{u}_k = \mathbf{\Phi}_k \, \hat{\mathbf{u}} = \overline{\mathbf{u}}_k, \tag{36}$$

with $k = 1, 2$, where $\overline{\mathbf{u}}_k$ denotes the specified displacement component. These equations are assembled into the global system (35).

ILMF naturally compute a symmetric and banded global system of equations, even though it generates the global system of equations in a node-by-node process, through equations (32) to (35). This generation process is systematically different from the one used in the traditional FEM that considers an element-by-element process to generate the global stiffness matrix.

A very short processing time to run the analysis is expected from ILMF, since the nodal stiffness matrix is computed, in equations (33), with only 4 integration points, one point for each segment of the local domain.

Another advantage is that the reduced integration leads to very accurate results. ILMF integration process plays an important role in the behavior of the numerical model, since it results in a reduction of the stiffness of the body, corresponding to an increase of the strain energy, which has the desirable effect of increasing the solution accuracy and, most important, presents no instabilities. It is important to highlight that this improved accuracy, generated by the reduced integration, has been already used in the standard FEM and other mesh free methods to prevent locking of fully integrated elements.

5.1 Convergence Analysis

The convergence analysis of ILMF can be done in a similar way of the convergence analysis of the standard displacement-assumed FEM, see Oliveira and Portela [2016].

A virtual displacement $\delta\mathbf{u}$, which is a continuous virtual variation of the displacement field $\mathbf{u}$ that actually settles in the body's domain Ω, is such a way that

$$\delta\mathbf{u} = \mathbf{0} \tag{37}$$

on Γ_u is where the prescribed kinematic boundary conditions cannot be varied.

In the local domain Ω_Q, with $\Gamma_Q = \Gamma_{Qi} \cup \Gamma_{Qt}$, consider the stress field $\boldsymbol{\sigma}$, that settles in the body's domain Ω. Now consider the work theorem, equation (17), with displacements defined as $\mathbf{u}^* = \delta\mathbf{u}$, leading to the theorem of virtual displacements that is

$$\int\limits_{\Gamma_Q - \Gamma_{Qt}} \mathbf{t}^T \delta\mathbf{u} \, \mathrm{d}\Gamma + \int\limits_{\Gamma_{Qt}} \overline{\mathbf{t}}^T \delta\mathbf{u} \, \mathrm{d}\Gamma = \int\limits_{\Omega_Q} \boldsymbol{\sigma}^T \delta\boldsymbol{\varepsilon} \, \mathrm{d}\Omega, \tag{38}$$

or simply

$$\int\limits_{\Gamma_Q} \mathbf{t}^T \delta\mathbf{u} \, \mathrm{d}\Gamma = \int\limits_{\Omega_Q} \boldsymbol{\sigma}^T \delta\boldsymbol{\varepsilon} \, \mathrm{d}\Omega, \tag{39}$$

in which $\delta\boldsymbol{\varepsilon}$ denotes the strain variation corresponding to the virtual displacement $\delta\mathbf{u}$.

The total potential energy functional in the local domain Ω_Q, is defined as

$$T = U + P, \tag{40}$$

in which the strain energy U is defined in terms of the respective density w as

$$U = \int\limits_{\Omega_Q} w \, \mathrm{d}\Omega = \int\limits_{\Omega_Q} \frac{1}{2} \, \boldsymbol{\sigma}^T \delta\boldsymbol{\varepsilon} \, \mathrm{d}\Omega \tag{41}$$

and the potential energy P of the external forces is defined as

$$P = -\int_{\Gamma_Q} \mathbf{t}^T \delta\mathbf{u}\, \mathrm{d}\Gamma. \tag{42}$$

The theorem of the total potential energy states that the elastic field that satisfies static admissibility, with the applied tractions, makes the total potential energy stationary, in the set of all elastic fields that satisfy kinematic admissibility, with the displacement constraints of the body. As a matter of fact, the first variation of the total energy T generates virtual variations of displacements $\delta\mathbf{u}$ and strains $\delta\boldsymbol{\varepsilon}$ and thus, equation (39) of the theorem of virtual displacements leads to a stationary condition

$$\delta T = \delta U + \delta P = \int_{\Omega_Q} \boldsymbol{\sigma}^T \delta\boldsymbol{\varepsilon}\, \mathrm{d}\Omega - \int_{\Gamma_Q} \mathbf{t}^T \delta\mathbf{u}\, \mathrm{d}\Gamma = 0, \tag{43}$$

that is a minimum, when the material stability of the body is assumed. Under these circumstances, the total potential energy theorem limits to a minimum value the total potential energy of the exact solution settled in the body. For now, consider that the work theorem (17), applied for the case of the elastic field that settles in the body, leads to $P = -2U$ and consequently $T = -U$. It can be seen that the minimum value of the total potential energy corresponds to a maximum value of the strain energy, which is, therefore, equivalent to a minimum value of the stiffness of the elastic field that settles in the body.

Discretization of the local form (24) is performed with the MLS approximation, generating a system of two algebraic equations. When more refined nodal distributions are considered, the approximated solution converge monotonically to the exact solution, likewise the standard FEM, provided the MLS approximation satisfies completeness and continuity, as FEM does.

As a final remark on the matter, it is important to point out that the presented reduced integration of the ILMF model does not lead to any sort of spurious instability. This behavior is a direct consequence of the use of 4 integration points to calculate the stiffness associated to each local node, on each boundary of the local domain. Therefore, this integration prevents the generation of spurious zero-energy modes, unlike nodal integration methods without stabilization.

5.2 Discretization Parameters

Local mesh free methods posses two key parameters that can greatly effect the analysis. The first is the size r_{Ω_s} of the compact support Ω_s, where shape functions are defined; and the second is the size r_{Ω_q} of the local integration domain Ω_q, where the work theorem is defined. Usually these parameters are heuristically determined by most authors employing mesh free methods.

For a node i, in a mesh free nodal distribution, these parameters can be defined, respectively as

$$r_{\Omega_s} = \alpha_s\, c_i \tag{44}$$

and

$$r_{\Omega_q} = \alpha_q\, c_i, \tag{45}$$

in which c_i denotes the distance of the reference node i, to the nearest node and α_s and α_q are arbitrary constant parameters that must be defined in any application.

Equations (44) and (45) show that the accuracy of a mesh free numerical application can be controlled an even improved through a proper specification of these discretization parameters α_s and α_q. In general, the discretization parameters are considered as $\alpha_s > 1.0$ and $\alpha_q < 1.0$, for regular node distributions on linear elastic problems.

The discretization parameter α_s, which is the size of the influence domain of each node, is directly determined by the compact supports, as seen in Section 2. The parameter is primarily linked to the accuracy of the mesh free formulation since it defines the total number of nodes required to build the respective nodal shape functions, in order to perform the MLS approximation of variables.

Meanwhile, The discretization parameter α_q, which is the local domain of integration of each node, where the stiffness matrix of each node is build, is primarily linked to the efficiency of the formulation. This domain must be within the solution domain, without intersecting the boundary of the body.

In order to further the efficiency of ILMF, proper values for these discretization parameters, α_s and α_q, are obtained automatically through a multi-objective optimization scheme.

6 Optimization Scheme for Discretization Parameters

The required background and terminology of multi-objective optimization, evolutionary algorithms and Pareto optimality are defined in optimization literature, formally introduced here by Hwang and Masud [1979], Sawaragi et al. [1985], Steuer [1986] and Ringuest [1992]. Some basic concepts and premises, important for comprehension of the optimization scheme formulated are presented here, for the sake of completeness.

6.1 Genetic Algorithms (GA)

GA belong to a broad category of evolutionary algorithms, which are optimization techniques that perform a search motivated by the principles of natural genetics and natural selection, proposed by Holland [1975]. They are known for performing a non-derivative global heuristic search and solve a wide rage of optimization problems, as presented by Kelner and Leonard [2004], McCall [2005] and Ebrahimnejad et al. [2015], for mesh free methods.

Basically, GA keep a population of individuals, in this case $\mathbf{P}(\mathbf{t})$, for generation $\mathbf{t}$. Each individual contains a possible solution to the posed problem. Each individual is programmed to give some measure of its fitness that will be evaluated later. Some of these individuals undergo stochastic transformations by means of genetic operations to form new individuals. This transformation can be a mutation, which creates new individuals by making changes in a single individual, or can be a crossover, which creates new individuals by combining parts from two others. The offspring $\mathbf{C}(\mathbf{t})$, the new individuals created, are then evaluated. A brand new population is formed by selecting the more fit individuals from the parent population and the offspring population. After several generations, or function evaluations, the algorithm converges to the best and most fit individual, which hopefully represents an optimal or sub-optimal solution to the problem, see Gen and Cheng [2000].

6.2 Symbiotic Organisms Search (SOS)

SOS is a powerful meta-heuristic optimization algorithm, also member of the broad category of evolutionary algorithms, originally introduced by Cheng and Prayogo [2014]. The method is described by a relationship between any two distinct species, from the Greek word for ”living together”.

The relationship between species can be either obligate, meaning the two organisms depend on each other for survival, or facultative, meaning the two organisms choose to cohabitate in a mutually beneficial but nonessential relationship. Mutualism, commensalism, and parasitism are

the most common symbiotic relationships found in nature. Mutualism denotes a symbiotic relationship between two different species in which both benefit, while commensalism is a symbiotic relationship between two different species in which one benefits and the other is unaffected or neutral. Parasitism is a symbiotic relationship between two different species in which one benefits and the other is actively harmed. Naturally, organisms develop symbiotic relationships as a strategy to adapt to changes in their environment. Symbiotic relationships may also help organisms increase fitness and survival advantage over the long-term.

Similar to other meta-heuristic algorithms, SOS is population-based and also uses a candidate solution to search for the optimal solution in the search space. Both GA and SOS provide a directed random search in complex landscapes. Genetic operations and symbiotic relationships perform essentially a blindfold search, while selection operators hopefully direct the search toward the desirable area of the solution space. The key feature of evolutionary algorithms is that they make a good balance between exploration and exploitation of the search space.

6.3 Objective Functions

The objective function provide the output required for the algorithm to evaluate a function. The optimization performance is highly dependable on well defined functions.

The first objective function results from the features of the parameter α_s. Consider any state of the elastic field that actually settles in the body, the strain energy U is given by

$$U = \int_{\Omega} \frac{1}{2} \boldsymbol{\sigma}^T \boldsymbol{\varepsilon} \, \mathrm{d}\Omega \tag{46}$$

and the potential energy P, of the external loads, given by

$$P = -\int_{\Gamma_t} \bar{\mathbf{t}}^T \mathbf{u} \, \mathrm{d}\Gamma, \tag{47}$$

can be used to handle the total potential energy T. The work theorem for the global domain of the body, results in $P = -2U$ and therefore $T = -U$, as well as $T = P/2$; for the actual elastic field of the body. It is clear that the minimum value of the total potential energy of the body corresponds to a minimum value of the potential energy P or a maximum value of the strain energy U.

There are two ways to handle the evaluation of the energy. The first is to evaluate the strain energy U of the body, which is computationally inefficient, since it requires the computation of the stress field for all nodal values and the evaluation of derivatives of shape functions that can degrade the numerical accuracy. The second is to evaluate the potential energy P, which is computationally more efficient, since only nodes with no-null applied external forces, albeit the ones at the static boundary, need to be evaluated. As it can be seen, this process is performed only at a few nodes and does not require the computation of derivatives of shape functions. Therefore, the objective function can be defined with the structural compliance C, as

$$C = \frac{1}{2} \int_{\Gamma_t} \bar{\mathbf{t}}^T \mathbf{u} \, \mathrm{d}\Gamma = -\frac{1}{2} P. \tag{48}$$

In the end, the minimum value of the potential energy P is equivalent to a minimum value of C that corresponds to a maximum value of $-C$.

The second objective function results from the features of the parameter α_q. The total area of integration of the body, the combined area of all local integration domains for each node, in

a nodal discretization, must be as close as possible to the geometrical area of the domain of the body. The objective function is defined by the resulting local domain area

$$A_q = \sum_{l=1}^{n} \frac{A_{\Omega_q}}{\Omega_q} \,, \tag{49}$$

in which A_{Ω_q} considers equation (45) to compute the total area of integration of each node and Ω_q is the total area of the domain of the body. Since the local domain can be defined with an arbitrary geometrical shape, usually a rectangular or a circular domain, that can intersect each other if necessary; the efficiency of the approximation is dependent on the geometry of the domain of the problem, which is adaptable through optimization.

6.4 Mathematical Formulation and Algorithm Implementation

The numerical problem optimization obtain optimal values for mesh free parameters α_s and/or α_q by minimizing the objective function through mesh free models, in this case ILMF, such that the geometrical constraints of the problem are satisfied. Three optimization schemes based on relative error, compliance and local domain are presented in the following.

The first multi-objective optimization scheme mathematical formulation is presented as

$$\begin{aligned}
\text{minimize} \quad & r_\varepsilon(\boldsymbol{\alpha_s}, \boldsymbol{\alpha_q}) \\
& r_u(\boldsymbol{\alpha_s}, \boldsymbol{\alpha_q}) \\
\text{subject to} \quad & \mathbf{e}(\boldsymbol{\alpha_s}) = {\alpha_s}^{min} \leq \alpha_s \leq {\alpha_s}^{max} \\
& \mathbf{e}(\boldsymbol{\alpha_q}) = {\alpha_q}^{min} \leq \alpha_q \leq {\alpha_q}^{max} \\
\text{where} \quad & \boldsymbol{\alpha_s} = (\alpha_{s1}, \alpha_{s2}, ..., \alpha_{sn}) \in \boldsymbol{\alpha} \\
& \boldsymbol{\alpha_q} = (\alpha_{q_1}, \alpha_{q_2}, ..., \alpha_{q_n}) \in \boldsymbol{\alpha} \,,
\end{aligned} \tag{50}$$

in which r_ε and r_u are, respectively the energy and displacement relative error, to be presented in section 8 and commonly used to measure numerical methods accuracy; ${\alpha_s}^{min}/{\alpha_q}^{min}$ and ${\alpha_s}^{max}/{\alpha_q}^{max}$ denote the minimum and the maximum allowable limits for the mesh free discretization parameters α_s and α_q, respectively.

The second multi-objective optimization scheme mathematical formulation is presented as

$$\begin{aligned}
\text{minimize} \quad & C(\boldsymbol{\alpha_s}) \\
& \text{CPU time}(\boldsymbol{\alpha_s}) \\
\text{subject to} \quad & \mathbf{e}(\boldsymbol{\alpha_s}) = {\alpha_s}^{min} \leq \alpha_s \leq {\alpha_s}^{max} \\
\text{where} \quad & \boldsymbol{\alpha_s} = (\alpha_{s1}, \alpha_{s2}, ..., \alpha_{sn}) \in \boldsymbol{\alpha} \,,
\end{aligned} \tag{51}$$

for GA and for SOS is defined in a mono-objective form as

$$\begin{aligned}
\text{minimize} \quad & C(\boldsymbol{\alpha_s}) \\
\text{subject to} \quad & \mathbf{e}(\boldsymbol{\alpha_s}) = {\alpha_s}^{min} \leq \alpha_s \leq {\alpha_s}^{max} \\
\text{where} \quad & \boldsymbol{\alpha_s} = (\alpha_{s1}, \alpha_{s2}, ..., \alpha_{sn}) \in \boldsymbol{\alpha} \,,
\end{aligned} \tag{52}$$

in which C is the structural compliance, presented in equation (48), and CPU time is the processing time required to generate and solve the global system of algebraic equations.

Finally, the third multi-objective optimization scheme mathematical formulation is presented as

$$\begin{aligned}
\text{minimize} \quad & A_q(\boldsymbol{\alpha_q}) \\
\text{subject to} \quad & \mathbf{e}(\boldsymbol{\alpha_q}) = {\alpha_q}^{min} \leq \alpha_q \leq {\alpha_q}^{max} \\
\text{where} \quad & \boldsymbol{\alpha_q} = (\alpha_{q_1}, \alpha_{q_2}, ..., \alpha_{q_n}) \in \boldsymbol{\alpha} \,,
\end{aligned} \tag{53}$$

in which A_q is the resulting local domain area, as presented in equation (49).

When mono-objective optimization is considered, the fitness function containing the mesh free formulation should accept a vector, whose length is the number of independent variables α_q, one for each node of the problem domain, and return a scalar value (A_q), the objective function. For multi-objective optimization, the same mesh free formulation should return a row vector of objective function values C, CPU time, r_ε and r_u. This process can be easily be extended to any local mesh free method from other authors.

Global variable is a function that can be used to perform multiple optimization processes and carry over the output of one optimization iteration phase, usually to optimize α_q first, to a second phase, where α_s can be optimized.

For GA, the proper values for population size, selection function, scaling function and etc, are different in each optimization scheme and will be properly addressed later. SOS requires only the population size and the maximum number of function evaluations, which is a key advantage of this method and will be addressed later.

Lastly, the automatic optimization of the discretization parameters is a combination of the features presented in section 6.3 into a single and unique routine, to automatically compute mesh free discretization parameters, α_s and α_q, in a robust and efficient way.

The optimization is divided in two distinct procedures, as presented in Figure 10.

In the first step, a single-objective optimization is performed, considering the mesh free model to evaluate A_q as an objective function. By the end of this process, the parameter α_q is optimized for n nodes of the model, as a vector $n \times 1$, which will be eventually introduced in the next iteration phase. In the second step, the parameter α_s is optimized as a scalar value, in a multi-objective optimization using the mesh free model to evaluate the compliance and the CPU time as objective functions.

The process is separated in two steps so that the parameter α_q is completely independent from α_s. As consequence, both can be calculated considering only the boundary conditions of the posed problem and the local domain of integration geometry. When combined, the routine guarantee that the integration will be effectively computed in the first phase and later that parameter α_s is effectively calculated considering the compliance and the CPU time, just to ensure that this optimization will result in fast computations, with no detriment for the solution accuracy.

As it can be seen from the optimization scheme, the fully automated routine can perform the optimization without the need of any analytical solution and for any bi-dimensional domain. Parallel environment can be included in the routine to improve the processing time of the optimization, which makes a robust tool to solve complex mesh free problems, although only ILMF and linear elastic problems are presented.

7 Linear Elastic Fracture Mechanics

Mixed-mode deformation of cracked plates can be effectively analyzed through the direct computation of the Stress Intensity Factor (SIF), carried out with the Singularity Subtraction Technique (SST). After implemented in a mesh free model, SST introduces the SIF as primary unknowns of the numerical model, by subtracting the crack tip singularity before the numerical solution.

Consider a two-dimensional cracked plate, with domain Ω and boundary $\Gamma = \Gamma_u \cup \Gamma_t$, in the absence of body forces, satisfies the equations

$$\mathbf{L}^T \boldsymbol{\sigma} = \mathbf{0} \tag{54}$$

$$\boldsymbol{\varepsilon} = \mathbf{L}\,\mathbf{u} \tag{55}$$

$$\boldsymbol{\sigma} = \mathbf{D}\,\boldsymbol{\varepsilon} \tag{56}$$

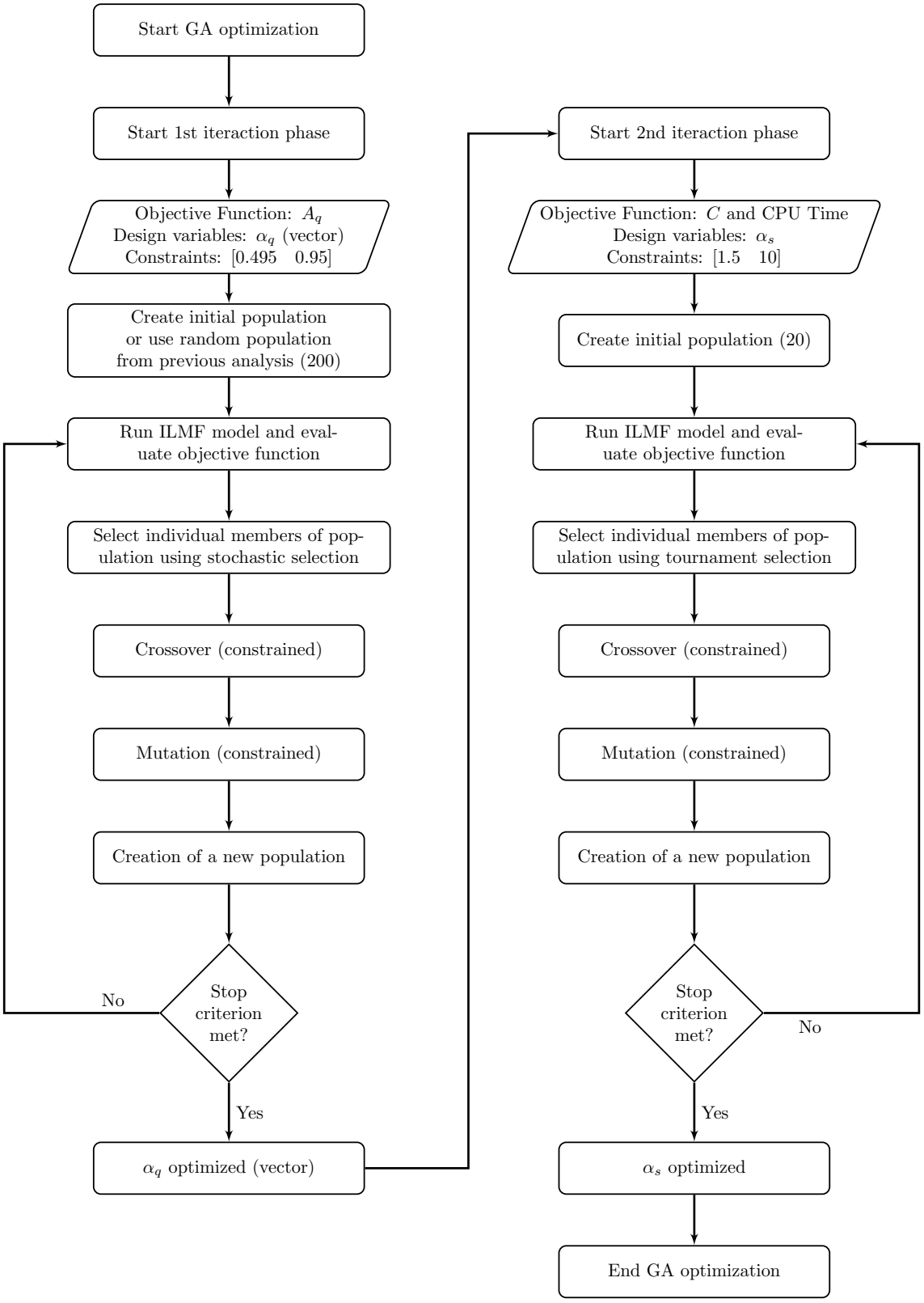

Figure 10: Optimization flowchart showing the required steps for the fully automated routine; the 1st step is presented on the left and the 2nd step is presented on the right.

in the domain Ω, with boundary conditions

$$\mathbf{u} = \overline{\mathbf{u}} \quad \text{on} \quad \Gamma_u \tag{57}$$

and

$$\mathbf{t} = \mathbf{n}\,\boldsymbol{\sigma} = \overline{\mathbf{t}} \quad \text{on} \quad \Gamma_t, \tag{58}$$

in which matrix $\mathbf{L}$ represents a differential operator; vectors $\boldsymbol{\sigma}$ represent the stresses and $\boldsymbol{\varepsilon}$ represent the strains; matrix $\mathbf{D}$ represents the elastic constants; vectors $\mathbf{u}$, $\mathbf{t}$ $\overline{\mathbf{u}}$ and $\overline{\mathbf{t}}$ represent, respectively displacements, tractions, prescribed values of displacements and tractions; and $\mathbf{n}$ denotes the components of the unit normal to the boundary, outwardly directed.

The singularity subtraction can be used to avoid inaccuracies due to unbounded stress at one point but with displacements bounded everywhere, in the numerical method. In linear elastic fracture mechanics, the stress field is singular at the crack tip and can be conveniently modified even before the solution is carried out with mesh free analysis. Based non the principle of superposition that allows linear behavior, the elastic field can be decomposed into a regular (R) and a singular (S) component as

$$\sigma_{ij} = (\sigma_{ij} - \sigma_{ij}^S) + \sigma_{ij}^S = \sigma_{ij}^R + \sigma_{ij}^S \tag{59}$$

and

$$u_i = (u_i - u_i^S) + u_i^S = u_i^R + u_i^S, \tag{60}$$

where $\sigma_{ij}^R = \sigma_{ij} - \sigma_{ij}^S$ and $u_i^R = u_i - u_i^S$ denotes the regular parts of the stress and displacement of the initial problem, respectively; σ_{ij}^S and u_i^S represents, respectively the stress and displacement of a particular solution of the initial problem that is the singular field in this case. The particular singular field, equations (59) and (60), regularize the initial elastic field when proper functions are used, since the stress σ_{ij}^R become non-singular.

The regularization strategy employed allow the analysis of the initial problem to be performed with the only regular elastic field, given by components σ_{ij}^R and u_i^R. Therefore, these components automatically satisfy the field equations, because they represent a particular solution of the initial problem. Hence, elasticity equations (54) to (56) are now written as

$$\mathbf{L}^T \boldsymbol{\sigma}^R = \mathbf{0} \tag{61}$$

$$\boldsymbol{\varepsilon}^R = \mathbf{L}\,\mathbf{u}^R \tag{62}$$

$$\boldsymbol{\sigma}^R = \mathbf{D}\,\boldsymbol{\varepsilon}^R \tag{63}$$

in domain Ω, with boundary conditions

$$\mathbf{u}^R = \overline{\mathbf{u}} - \mathbf{u}^S \quad \text{on} \quad \Gamma_u \tag{64}$$

and

$$\mathbf{t}^R = \overline{\mathbf{t}} - \mathbf{t}^S \quad \text{on} \quad \Gamma_t. \tag{65}$$

Note that, except for boundary conditions from equations (64) and (65), this regularized problem is governed by the same equations of the initial problem, where the additional terms, components $\mathbf{u}^S$ and $\mathbf{t}^S$ of a singular particular solution of the initial problem, are included.

The singular field around the crack tip, represented by components of the particular solution σ_{ij}^S and u_i^S in equations (59) and (60), can be defined through the first term of the Williams [1952] eigenexpansion, derived for a semi-infinite edge crack. The stress components are

$$\sigma_{11}^S = \frac{K_I}{\sqrt{2\pi r}} \cos\frac{\theta}{2}\left(1 - \sin\frac{\theta}{2}\sin\frac{3\theta}{2}\right) + \frac{K_{II}}{\sqrt{2\pi r}} \sin\frac{\theta}{2}\left(2 + \cos\frac{\theta}{2}\cos\frac{3\theta}{2}\right), \tag{66}$$

$$\sigma_{22}^S = \frac{K_I}{\sqrt{2\pi r}} \cos\frac{\theta}{2}\left(1 + \sin\frac{\theta}{2}\sin\frac{3\theta}{2}\right) - \frac{K_{II}}{\sqrt{2\pi r}} \sin\frac{\theta}{2}\cos\frac{\theta}{2}\cos\frac{3\theta}{2} \tag{67}$$

and

$$\sigma_{12}^S = \frac{K_I}{\sqrt{2\pi r}} \cos\frac{\theta}{2}\sin\frac{\theta}{2}\cos\frac{3\theta}{2} + \frac{K_{II}}{\sqrt{2\pi r}} \cos\frac{\theta}{2}\left(1 - \sin\frac{\theta}{2}\sin\frac{3\theta}{2}\right) \tag{68}$$

and the displacement components are

$$\begin{aligned} u_1^S = &\frac{K_I}{4\mu}\sqrt{\frac{r}{2\pi}}\left[(2\kappa - 1)\cos\frac{\theta}{2} - \cos\frac{3\theta}{2}\right] + \\ &+\frac{K_{II}}{4\mu}\sqrt{\frac{r}{2\pi}}\left[(2\kappa + 3)\sin\frac{\theta}{2} + \sin\frac{3\theta}{2}\right] \end{aligned} \tag{69}$$

and

$$\begin{aligned} u_2^S = &\frac{K_I}{4\mu}\sqrt{\frac{r}{2\pi}}\left[(2\kappa + 1)\sin\frac{\theta}{2} - \sin\frac{3\theta}{2}\right] + \\ &+\frac{K_{II}}{4\mu}\sqrt{\frac{r}{2\pi}}\left[(2\kappa - 3)\cos\frac{\theta}{2} + \cos\frac{3\theta}{2}\right], \end{aligned} \tag{70}$$

where K_I and K_{II} represent the SIF, respectively of the opening and sliding modes; the constant $\kappa = 3 - 4\nu$ is established for plain strain and $\kappa = (3 - \nu)/(1 + \nu)$ for plain stress, in which ν is Poisson's ratio; and constant μ is the shear modulus. A polar coordinate reference system (r, θ), centered at the crack tip, is defined such that $\theta = 0$ is the crack axis, ahead of the crack tip, as Figure 11 represents.

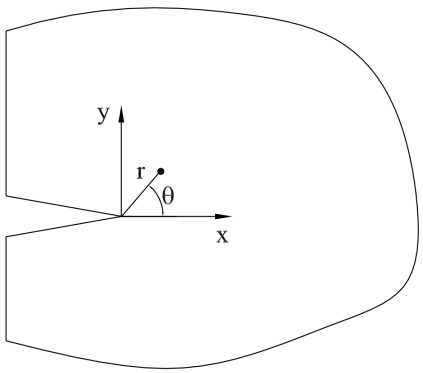

Figure 11: Polar coordinate reference system for William's singular particular solution.

It is noticeable that the order $r^{-1/2}$ of the stress field becomes singular when r tends to zero. Note also that rigid-body terms are not included in the displacement field, which leads to null components at the crack tip. As demonstrated by Caicedo and Portela [2015], the first term of the William's eigenexpansion, derived for an edge crack, can also be used to represent the elastic field around the crack-tip, where the singular behavior of the stress field is dominant, for the case of internal piecewise-flat multi-cracked finite plates, under mixed-mode deformation.

Traction components are defined, at a boundary point, through the singular stress of equations (66) to (68), as follow

$$\mathbf{t}^S = \begin{bmatrix} t_1^S \\ t_2^S \end{bmatrix} = \begin{bmatrix} \sigma_{11}^S & \sigma_{21}^S \\ \sigma_{12}^S & \sigma_{22}^S \end{bmatrix} \begin{bmatrix} n_1 \\ n_2 \end{bmatrix} = \begin{bmatrix} g_{11} & g_{12} \\ g_{21} & g_{22} \end{bmatrix} \begin{bmatrix} K_I \\ K_{II} \end{bmatrix} = \mathbf{g}\ \mathbf{k}, \tag{71}$$

where n_i refers to the i-th component of the unit normal to the boundary, outwardly directed; functions $g_{ij} = g_{ij}(r^{-1/2}, \theta)$ were introduced for a convenient notation of equations (66) to (68) and the vector $\mathbf{k}$ contains the SIF.

The displacement field, presented in equations (69) and (70), similar to the stress field, can be defined in a vector form as

$$\mathbf{u}^S = \begin{bmatrix} u_1^S \\ u_2^S \end{bmatrix} = \begin{bmatrix} f_{11} & f_{12} \\ f_{21} & f_{22} \end{bmatrix} \begin{bmatrix} K_I \\ K_{II} \end{bmatrix} = \mathbf{f}\ \mathbf{k}, \tag{72}$$

where functions $f_{ij} = f_{ij}(r^{1/2}, \theta)$ are a convenient notation of equations (69) and (70).

7.1 Mesh free Formulation for Fracture Mechanics

Generally, an analytical solution of the regularized problem, equations (61) to (63), with boundary conditions (64) and (65), are not available for practical problems. Therefore, numerical methods, in this case ILMF, are employed and considered to obtain the approximate solution.

Consider the domain Ω_Q associated with the node $Q \in \Omega_Q \cup \Gamma_Q$, the equilibrium equations (23) are now rewritten as

$$\int_{\Gamma_Q - \Gamma_{Qt}} \mathbf{t}^R \, \mathrm{d}\Gamma = - \int_{\Gamma_{Qt}} \left(\bar{\mathbf{t}} - \mathbf{t}^S \right) \, \mathrm{d}\Gamma, \tag{73}$$

in which the static boundary conditions (65), of the regularized problem, are considered.

Therefore, for a linear reduced integration, along each boundary segment of the local domain, equation (73) simply leads to

$$\frac{L_i}{n_i} \sum_{j=1}^{n_i} \mathbf{t}^R_{\mathbf{x}_j} = -\frac{L_t}{n_t} \sum_{k=1}^{n_t} \bar{\mathbf{t}}_{\mathbf{x}_k} + \int_{\Gamma_{Qt}} \mathbf{t}^S \, \mathrm{d}\Gamma, \tag{74}$$

in which n_i and n_t denote the total number of integration points, or boundary segments, defined on, respectively the interior local boundary $\Gamma_{Qi} = \Gamma_Q - \Gamma_{Qt} - \Gamma_{Qu}$, with length L_i, and the local static boundary Γ_{Qt}, with length L_t.

Now, consider a mesh free discretization of the domain Ω, with circular or rectangular local domains, as Figure 7 schematically represents. The MLS approximation is used to perform the discretization of the local form, equation (74), in terms of the unknown nodal parameters $\hat{\mathbf{u}}^R$, which leads to the system of two linear algebraic equations

$$\frac{L_i}{n_i} \sum_{j=1}^{n_i} \mathbf{n}_{\mathbf{x}_j} \mathbf{D} \mathbf{B}_{\mathbf{x}_j} \hat{\mathbf{u}}^R = - \frac{L_t}{n_t} \sum_{k=1}^{n_t} \bar{\mathbf{t}}_{\mathbf{x}_k} + \int_{\Gamma_{Qt}} \mathbf{g} \, \mathrm{d}\Gamma \ \mathbf{k} \tag{75}$$

that can be written as

$$\mathbf{K}_Q \, \hat{\mathbf{u}}^R + \mathbf{G}_Q \, \mathbf{k} = \mathbf{F}_Q, \tag{76}$$

in which the stiffness matrix $\mathbf{K}_Q$ is given by

$$\mathbf{K}_Q = \frac{L_i}{n_i} \sum_{j=1}^{n_i} \mathbf{n}_{\mathbf{x}_j} \mathbf{D} \mathbf{B}_{\mathbf{x}_j}, \tag{77}$$

of the order $2 \times 2n$, where n is the number of nodes inside the influence domain of the node Q. Matrix $\mathbf{G}_Q$, of the order 2×2, computed from equations (71), is presented as

$$\mathbf{G}_Q = - \int_{\Gamma_{Qt}} \mathbf{g} \, \mathrm{d}\Gamma \tag{78}$$

and $\mathbf{F}_Q$ is the force vector given by

$$\mathbf{F}_Q = -\frac{L_t}{n_t}\sum_{k=1}^{n_t}\bar{\mathbf{t}}_{\mathbf{x}_k}. \tag{79}$$

In the case of an interior node, it can be seen that matrix $\mathbf{G}_Q$ and vector $\mathbf{F}_Q$ are null. For a problem with a total of N nodes, the assembly of equations (76) for all M interior and static-boundary nodes generates the global system of $2M \times (2N+2)$ equations

$$\mathbf{K}\,\hat{\mathbf{u}}^R + \mathbf{G}\,\mathbf{k} = \mathbf{F}. \tag{80}$$

On the kinematic boundary, the $N-M$ nodes are used to generate the remaining equations of the model, adding the kinematic boundary conditions of the regularized problem, equations (64). Thus, for a kinematic-boundary node, the boundary conditions of the regularized problem are enforced by a direct interpolation method as

$$\mathbf{u}_k^R = \mathbf{\Phi}_k\,\hat{\mathbf{u}}^R = \overline{\mathbf{u}}_k - \mathbf{u}_k^S = \overline{\mathbf{u}}_k - \mathbf{f}_k\,\mathbf{k}, \tag{81}$$

with $k = 1, 2$, where $\overline{\mathbf{u}}_k$ denotes the specified displacement component and $\mathbf{u}_k^S = \mathbf{f}_k\,\mathbf{k}$ is the displacement component of the particular singular solution, derived from equations (72). Equations (81) are written in the same form of equations (76), for a point Q, as

$$\mathbf{K}_{Q_k}\,\hat{\mathbf{u}}^R + \mathbf{G}_{Q_k}\,\mathbf{k} = \mathbf{F}_{Q_k}, \tag{82}$$

in which $\mathbf{K}_{Q_k}$ is now given by

$$\mathbf{K}_{Q_k} = \mathbf{\Phi}_k, \tag{83}$$

while $\mathbf{G}_{Q_k}$ is given by

$$\mathbf{G}_{Q_k} = \mathbf{f}_k \tag{84}$$

and $\mathbf{F}_{Q_k}$ is given by

$$\mathbf{F}_{Q_k} = \overline{\mathbf{u}}_k. \tag{85}$$

Local equations (82) are assembled into the global system of equations (80) which results in

$$\begin{bmatrix}\mathbf{K} & \mathbf{G}\end{bmatrix}\begin{bmatrix}\hat{\mathbf{u}}^R \\ \mathbf{k}\end{bmatrix} = \begin{bmatrix}\mathbf{F}\end{bmatrix}, \tag{86}$$

in which $\mathbf{K}$ is a matrix of the order $2N \times 2N$, $\mathbf{G}$ is a matrix of the order $2N \times 2$ and $\mathbf{F}$ is a vector of the order $2N$; the unknowns are the vector $\hat{\mathbf{u}}^R$, of the order $2N$, and the vector $\mathbf{k}$ of the order 2. Is important to highlight that this global system of equations introduce the SIF K_I and K_{II}, in the vector $\mathbf{k}$, as additional unknowns of the numerical problem. Hence, to end with a well-posed problem, additional constraint equations are necessary, , one for each mode considered in the analysis, in order to obtain a unique solution. These additional constraint are defined as two rows that goes into to the bottom of the system of equations (86).

Considering the regularized problem, the required additional constraints enforce the singularity cancellation. The regular displacement components or the regular stress components can be canceled out at the crack tip, that is

$$u_i^R = 0 \;\Rightarrow\; u_i = u_i^S, \tag{87}$$

or

$$\sigma_{ij}^R = 0 \;\Rightarrow\; \sigma_{ij} = \sigma_{ij}^S \tag{88}$$

which ensure that, at the crack tip, the initial problem is singular.

In order to be more effective, the additional constraints must be defined in terms of the unknown regularized MLS nodal parameters of $\hat{\mathbf{u}}^R$. Null displacement components are obtained from the use of conditions (87) at the crack tip, which can over-constrain the initial problem, because the singular displacement components, equations (69) and (70), do not include rigid-body terms. Thus, can not be used as the required additional constraints.

Conditions (88) can be redefined, in terms of the respective traction components at the crack tip, as

$$t_j^R = \sigma_{ij}^R n_i = 0 \;\Rightarrow\; t_j = t_j^S, \tag{89}$$

where n_i denotes the unit normal components of the crack faces, as represented schematically in Figure 12. After the MLS approximation, conditions (89), defined at the crack tip $\mathbf{x}_{tip}$, can be

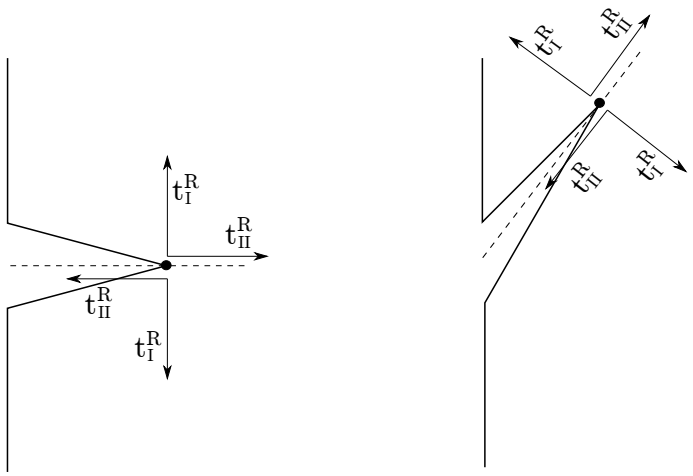

Figure 12: Crack tip tractions of the regularized elastic field.

defined as

$$\mathbf{t}_{\mathbf{x}_{tip}}^R = \mathbf{n}_{\mathbf{x}_{tip}} \mathbf{D}\, \mathbf{B}_{\mathbf{x}_{tip}}\; \hat{\mathbf{u}}^R = \mathbf{0}, \tag{90}$$

or

$$\mathbf{C}\; \hat{\mathbf{u}}^R = \mathbf{0}, \tag{91}$$

in which matrix $\mathbf{C}$ is written as

$$\mathbf{C} = \mathbf{n}_{\mathbf{x}_{tip}} \mathbf{D}\, \mathbf{B}_{\mathbf{x}_{tip}}. \tag{92}$$

Moreover, the additional constraints (92) can now be added into the global system of equations (86), leading to the final system of equations of the order $(2N+2) \times (2N+2)$

$$\begin{bmatrix} \mathbf{K} & \mathbf{G} \\ \mathbf{C} & \mathbf{0} \end{bmatrix} \begin{bmatrix} \hat{\mathbf{u}}^R \\ \mathbf{k} \end{bmatrix} = \begin{bmatrix} \mathbf{F} \\ \mathbf{0} \end{bmatrix}, \tag{93}$$

which can be solved without any inconsistency.

8 Numerical Results

Some numerical results are presented in this section to illustrate the accuracy and efficiency of the ILMF numerical formulation, under linear elastic problems and linear elastic fracture mechanics problems, on two-dimensional spaces. The results are compared with the analytical solution and the MLPG-5, presented by Atluri and Shen [2002], from now on refereed as MLPG; and for some

applications with the MLPG-FVM, introduced by Atluri et al. [2004] and the EFG, presented by Belytschko et al. [1994b].

For error estimation, important to measure the accuracy of numerical methods, displacement and energy L_2 norms can be used, respectively as

$$\|\mathbf{u}\| = \left[\int_{\Omega} \mathbf{u}^T \mathbf{u}\, \mathrm{d}\Omega\right]^{1/2} \tag{94}$$

and

$$\|\boldsymbol{\varepsilon}\| = \left[\frac{1}{2}\int_{\Omega} \boldsymbol{\varepsilon}^T \mathbf{D}\, \boldsymbol{\varepsilon}\, \mathrm{d}\Omega\right]^{1/2}. \tag{95}$$

Moreover, the relative errors, respectively for $\|\mathbf{u}\|$ and $\|\boldsymbol{\varepsilon}\|$ are given by

$$r_u = \frac{\|\mathbf{u}_{num} - \mathbf{u}_{exact}\|}{\|\mathbf{u}_{exact}\|} \tag{96}$$

and

$$r_\varepsilon = \frac{\|\boldsymbol{\varepsilon}_{num} - \boldsymbol{\varepsilon}_{exact}\|}{\|\boldsymbol{\varepsilon}_{exact}\|}. \tag{97}$$

All the routines and numerical applications were compared when using MATLAB 2015a on an Intel Core I7-4700MQ computer with CPU of 2.4GHz and 16 GB of RAM.

8.1 Benchmark Problem 1 – Cantilever-Beam

First, consider a beam of dimensions $L \times D$ and of unit depth, subjected to a parabolic traction at the free end as shown in Figure 13.

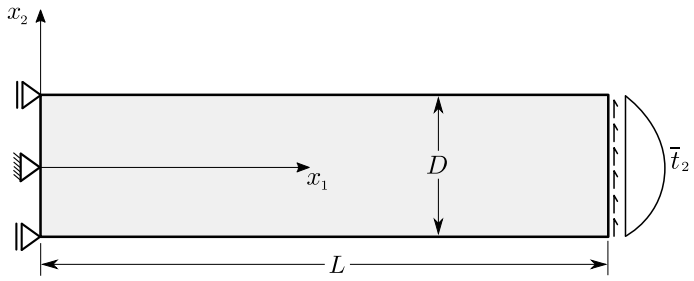

Figure 13: Timoshenko cantilever beam.

The beam is assumed in a plane stress state and the parabolic traction is given by

$$\overline{t}_2(x_2) = -\frac{P}{2I}\left(\frac{D^2}{4} - x_2^2\right), \tag{98}$$

where $I = D^3/12$ is the moment of inertia. The exact displacement components for this problem are given by

$$u_1(x_1, x_2) = -\frac{P x_2}{6EI}\left[(6L - 3x_1)x_1 + (2+\nu)\left(x_2^2 - \frac{D^2}{4}\right)\right] \tag{99}$$

and

$$u_2(x_1, x_2) = \frac{P}{6EI}\left[3\nu x_2^2(L - x_1) + (4 + 5\nu)\frac{D^2 x_1}{4} + (3L - x_1)x_1^2\right] \tag{100}$$

and the exact stress components are given by

$$\sigma_{11}(x_1, x_2) = -\frac{P(L - x_1)x_2}{I}, \quad \sigma_{12}(x_1, x_2) = -\frac{P}{2I}\left(\frac{D^2}{4} - x_2^2\right) \text{ and } \sigma_{22}(x_1, x_2) = 0. \tag{101}$$

Material properties are taken as Young′s modulus $E = 3.0 \times 10^7$ and the Poisson′s ratio $\nu = 0.3$ and the beam dimensions are $D = 12$ and $L = 48$. The shear force applied is $P = 1000$. To solve this problem, a regular nodal distribution, represented in Figure 14, was considered with

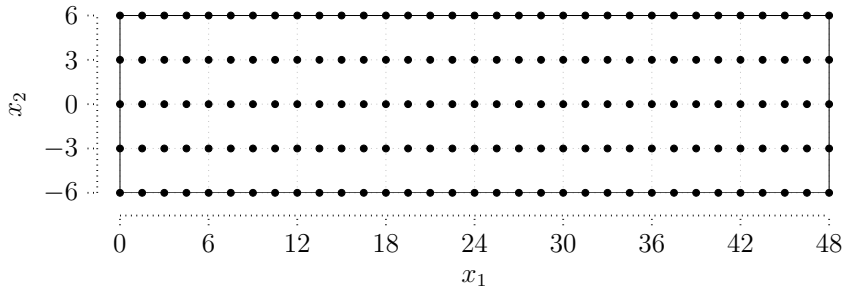

Figure 14: The regular nodal distribution of the cantilever-beam discretization with $33 \times 5 = 165$ nodes.

a nodal distribution of $33 \times 5 = 165$ nodes. The discretization parameters, α_s and α_q, need to be properly defined, through equations (44) and (45), in order to obtain a stable and accurate solution. for the applications presented in this first example, these parameters are heuristically defined as $\alpha_s = 3.0 \sim 4.5$ and $\alpha_q = 0.5 \sim 0.6$.

A first-order polynomial basis was considered in MLS approximation. Rectangular local domains Ω_q of each node were considered, with 1 point for ILMF integration and 10 Gauss-quadrature points to integrate the MLPG, placed along the sides of the local domain, as schematically represented in Figure 15.

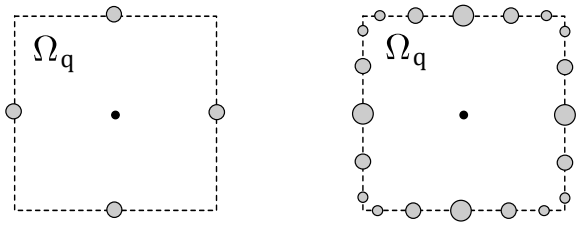

(a) ILMF (b) MLPG

Figure 15: Integration points placed on each side of the local domain Ω_q, to compute the equilibrium equations of ILMF and MLPG.

8.1.1 Displacement and Stress

The displacements resulting from this analysis, represented in Figure 16, show very good agreement with the results of the analytical solution. Albeit this relatively coarse nodal configuration, relative errors of $r_u = 6.33 \times 10^{-4}$ and $r_\epsilon = 7.51 \times 10^{-5}$ were obtained with ILMF. Stresses, computed at the center of the beam that is $x_1 = L/2$ and $x_2 \in [-D/2, D/2]$, also present excellent agreement with the results of the exact solution, as shown in Figure 17.

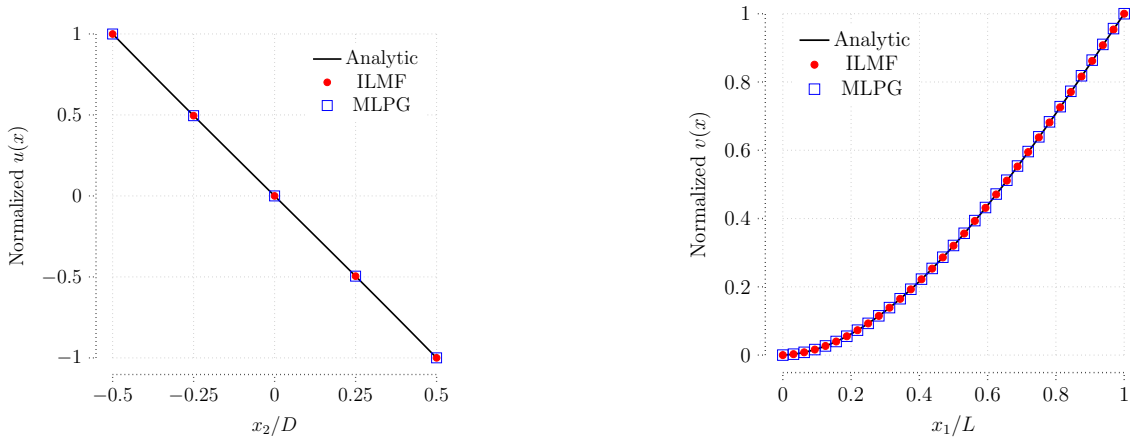

(a) for $x_2 = 0$ (b) for $x_1 = L/2$

Figure 16: Normalized displacements of the beam with nodal distribution of $33 \times 5 = 165$ nodes.

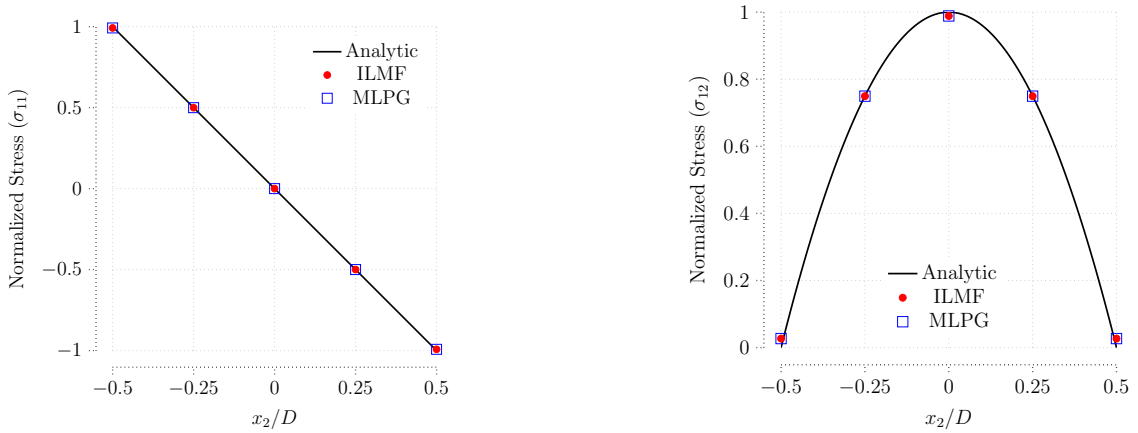

Figure 17: Stress distribution for $\mathbf{x_1 = L/2}$ and $\mathbf{x_2 \in [-D/2, D/2]}$ of the beam with nodal distribution of $33 \times 5 = 165$ nodes.

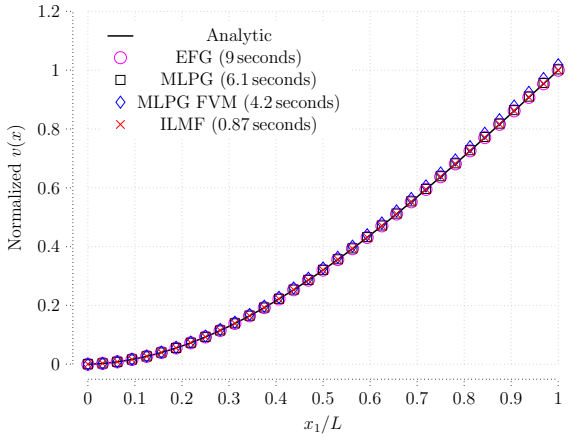

Figure 18: Normalized displacements of different mesh free methods, along with CPU time in seconds, for nodal distribution of $33 \times 5 = 165$ nodes.

When compared to other local mesh free methods, ILMF obtained a good accuracy and efficiency, as shown in Figure 18, where the processing time is also present. The EFG considered 10 Gauss-quadrature points on each background cell and the MLPG FVM considered 10 Gauss-quadrature points distributed on the local domain, for this application. In this initial performance analysis, the fastest computation is obtained with the ILMF, which is 21% faster than the MLPG FVM, the second best result.

8.1.2 Reduced Integration performance

One of the key advantages of ILMF is the reduced integration that differentiates it from other mesh free numerical methods. The linear reduced integration employed by ILMF consider only 1 point per segment of the local boundary. If necessary, additional integration points can be placed by subdividing a boundary segment in identical segments, which leads to equally-spaced integration points. for the general case, it is necessary to assess the performance of ILMF, driven by the location of integration points on each boundary of the local domain. Figure 19 shows the behavior

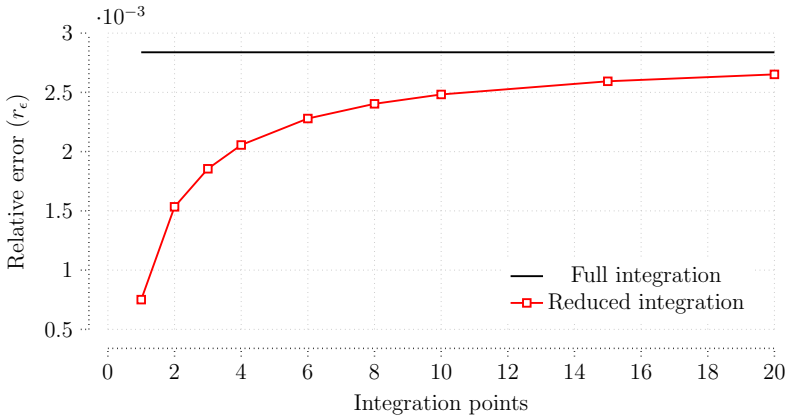

Figure 19: ILMF and MLPG relative error r_ϵ, as a function of the number of equally-spaced integration points, on each boundary of the respective local domain, for a regular distribution of $33 \times 5 = 165$ nodes.

of the relative error r_ϵ of ILMF, as a function of the number of integration points, for the nodal

distribution of $33 \times 5 = 165$ nodes; for comparison, the relative error of MLPG, computed with 10 Gauss points, is also plotted. It can be seen that the relative error of ILMF always monotonically converge for the relative error of MLPG with full integration. Physically, this means that the MLPG approximation always leads to stiffer models than the ones of the ILMF approximation. The minimum value of the error is always obtained for 1 collocation point. This is a very important result that evidences that ILMF linear reduced integration leads to better results than those obtained with the MLPG full integration.

Another test was required to assess the influence of the discretization on the accuracy of ILMF, regarding the number of integration points along the boundaries of the local domain. Therefore, four regular distributions of $13 \times 4 = 52$, $65 \times 9 = 585$, $97 \times 13 = 1261$ and $129 \times 17 = 2193$ nodes were considered. he results obtained for the ILMF relative error r_ϵ, as a function of the integration points are presented in Figure 20, where it can be seen that the accuracy of ILMF increases with

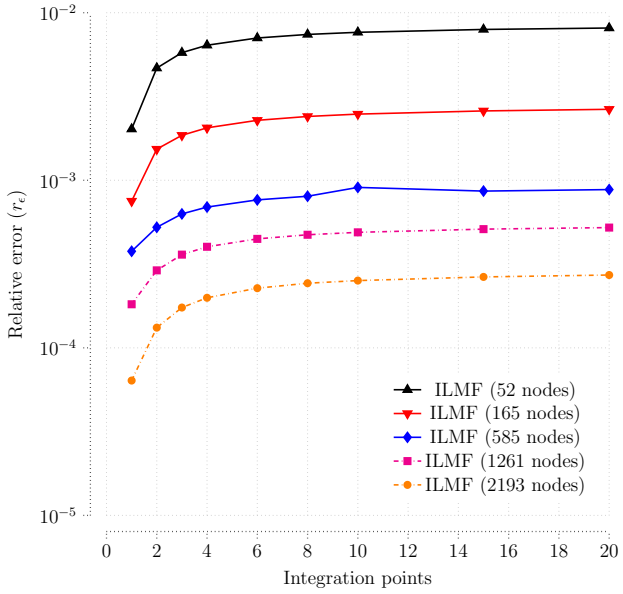

Figure 20: ILMF relative error r_ϵ, for beam discretizations with $13 \times 4 = 52$, $65 \times 9 = 585$, $97 \times 13 = 1261$ and $129 \times 17 = 2193$ nodes, as a function of the equally-spaced integration points, on the boundaries of the respective local domain.

the total number of nodes of the discretization, as expected. Effectively, the overall relative error of ILMF decreases with finer nodal distributions, requiring only one integration point along each boundary to obtain the most accurate results. This is a very important result that evidences that ILMF is a very efficient method.

The accuracy of the proposed method when considering higher order polynomial basis need to be addressed, hence another test was carried out. For this case, three regular distributions of $13 \times 4 = 52$, $33 \times 5 = 165$ and $65 \times 9 = 585$ nodes were considered. The results, presented in Figure 21 clearly evidence the accuracy of the reduced integration even for high-order polynomial basis, providing a stable convergence rate regardless of the polynomial basis.

8.1.3 Irregular Nodal Distributions

Irregularity on a nodal distribution can be introduced into a regular distribution by randomly changing nodal coordinates, within a local domain of integration. This procedure, referred to as level-1 of irregularity, can be addressed through an arbitrary variable c_n that varies in the range from 0.0 to 0.4, where $c_n = 0.4$ corresponds to a maximum irregularity, as seen in Liu [2003].

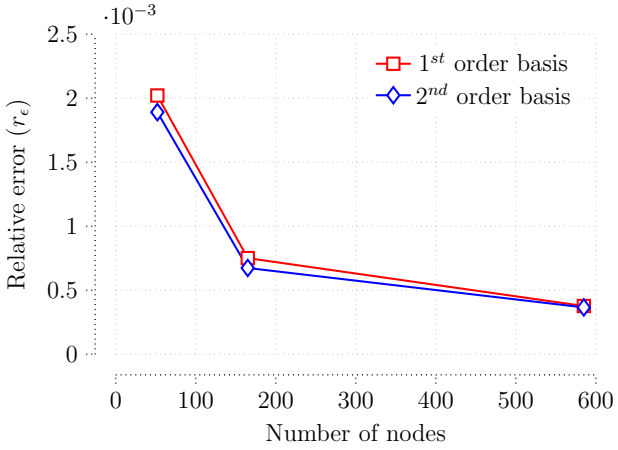

Figure 21: ILMF relative error r_ϵ for the beam modal distribution of $13 \times 4 = 52$, $33 \times 5 = 165$ and $65 \times 9 = 585$ nodes, as a function of the number of nodes, considering a complete set of first and second order polynomial basis for the MLS approximation.

Irregularity of a nodal distribution can greatly affect the solution accuracy, since it has a direct influence in the size of the compact support α_s and the size of the local integration domain α_q. If the distance between nodes is too large, the support regions around each node do not intersect with each other, thus providing no output. In the other extreme, if the distance between nodes is too small, too many nodes are crammed, thus losing the local character of the approximation. For this specific example, these parameters are heuristically defined as $\alpha_s = 2.11$ and $\alpha_q = 0.5$.

Three nodal distributions of the beam discretization, with 189 nodes and level-1 of irregularity, with two different irregularity configurations, regarding the boundary nodes, are presented in Figure 22. In configuration A, only interior nodes have an irregular distribution, as presented by Liu [2003], while in configuration B, all nodes are irregularly distributed. Results for this level-1 irregularity are presented in Figure 23, where it can be seen that ILMF obtained stable results with a high accuracy, even for mild irregular nodal distributions.

The generation of nodal distributions with severe irregularity are divide in two major steps. First, the coordinates of a nodal regular distribution are randomly changed, allowing each node to move outside the respective local domain of integration. Second, each local domain is regenerated, in order to include the new location of the respective node, by considering the middle of the distance between the node and its neighboring nodes. This procedure, referred to as level-2 of irregularity, can be addressed through an arbitrary variable c_n that now varies in the range from 0.0 to 0.9, where $c_n = 0.9$ corresponds to a maximum irregularity, as seen in Liu [2003].Figure 24 represent three nodal distributions of the beam discretization, with 55 and 189 nodes with irregularity of level-2 for interior nodes. Due to the high irregularity, $\alpha_s = 12.00$ was considered for this case.

Figure 25 show the results obtained for irregular nodal distributions of level-2, preserving the high accuracy level obtained by ILMF. These results demonstrate that high irregularities require higher values for parameter α_s, in order to keep the accuracy of results. The results show that ILMF is a reliable mesh free numerical model, since even with nodal distributions with severe irregularities, the solution is still accurate.

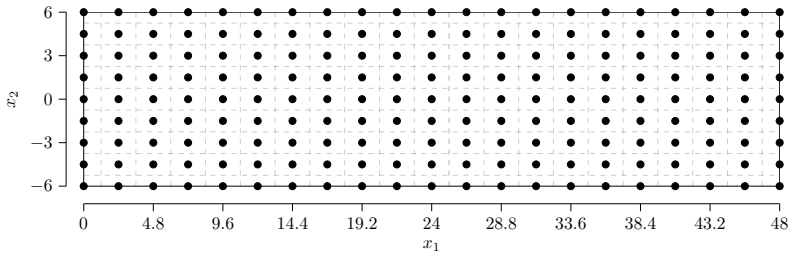

(a) $c_n = 0.0$

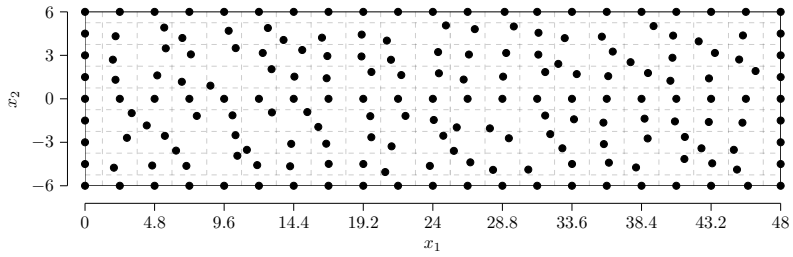

(b) $c_n = 0.4$, configuration A

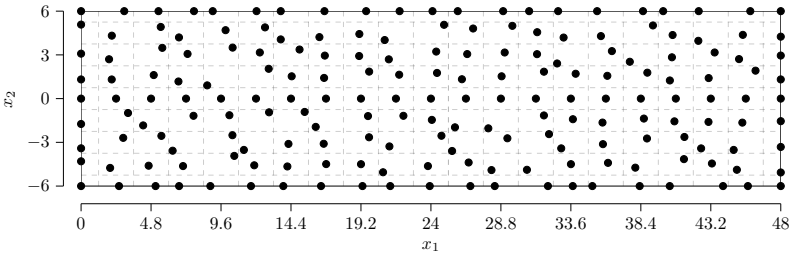

(c) $c_n = 0.4$, configuration B

Figure 22: Nodal distributions of the beam discretization with 189 nodes and level-1 of irregularity.

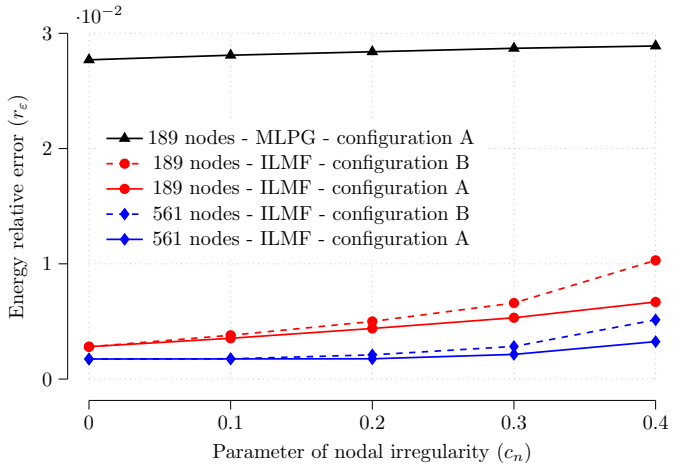

(a) ILMF and MLPG

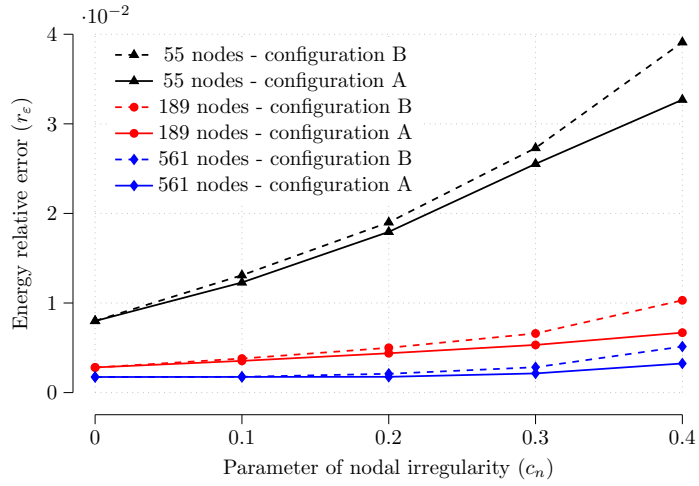

(b) ILMF

Figure 23: ILMF and MLPG energy error, as a function of the irregularity parameter c_n, obtained with irregular nodal distributions with 189 and 561 nodes of the beam discretization.

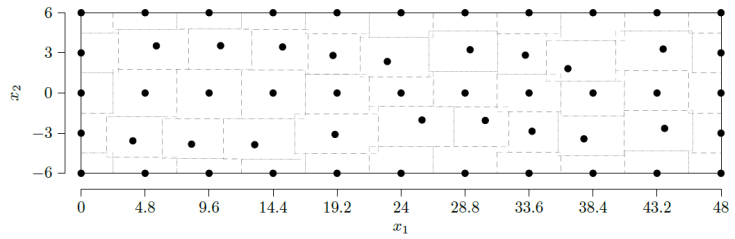

(a) 55 nodes with $c_n = 0.4$

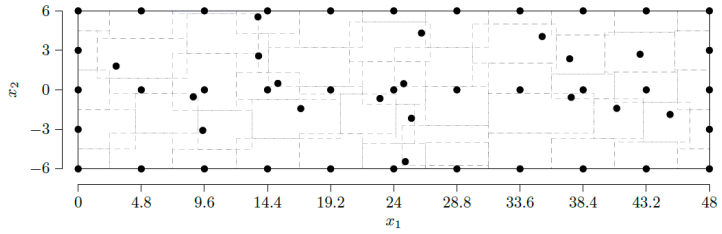

(b) 55 nodes with $c_n = 0.8$

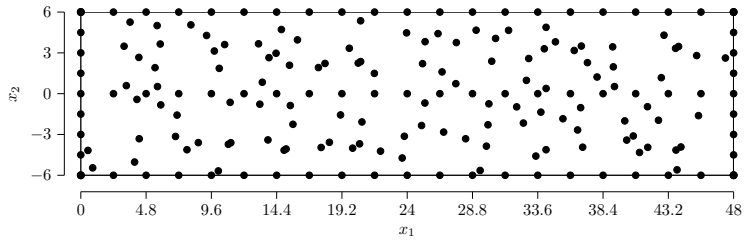

(c) 189 nodes with $c_n = 0.8$

Figure 24: Nodal distributions of the beam discretization, with 55 and 189 nodes with level-2 irregularity.

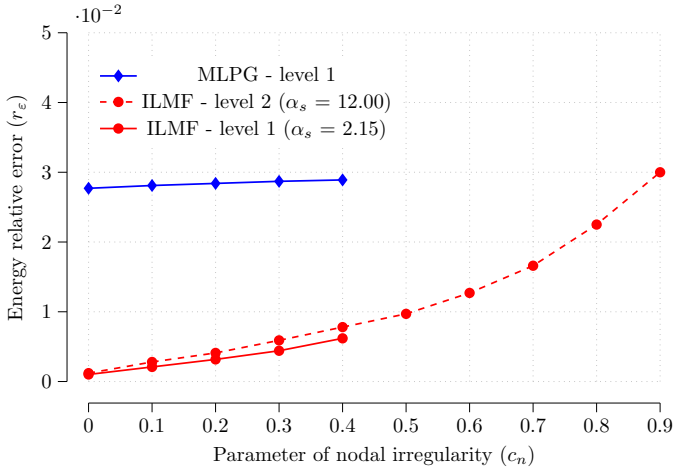

(a) Level-1 and level-2 irregularities

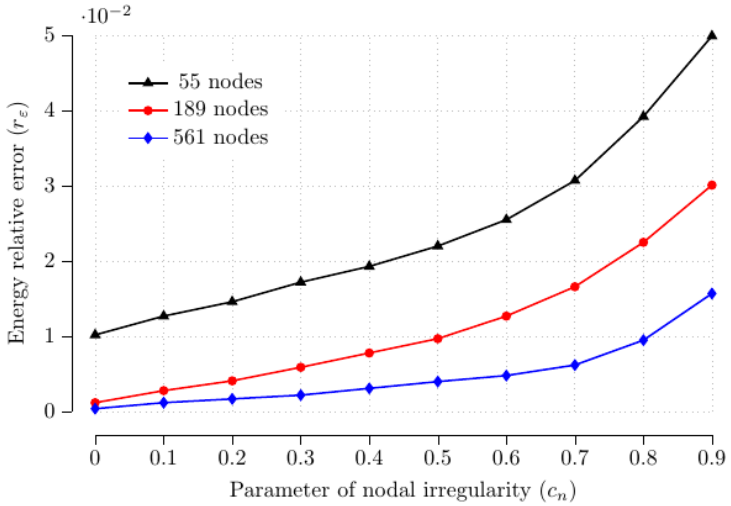

(b) ILMF with level-2 irregularities

Figure 25: Energy relative error of ILMF and MLPG, as a function of the irregularity parameter c_n, obtained with irregular nodal distributions of the beam discretization.

8.1.4 Automatic Parameter Optimization

Several optimization schemes are presented with different objective functions. In the end, the ultimate optimization approach computes automatically the ILMF discretization parameters, α_s and α_q, in a very efficient way.

In the first scheme, GA is implemented in order to minimize the CPU time and the relative error r_ε and r_u, defined as objective functions for this approach. Tha main goal is to asses the performance of the optimization process related to the accuracy and the computational effort. Only the major computational cost that is the cost of generating and solving the global system of algebraic equations, was measured. The decision variables, α_s and α_q, are defined as continuous in the intervals, respectively

$$\alpha_s = [1.1\ 10] \quad and \quad \alpha_q = [0.1\ 0.9]. \tag{102}$$

There is a strong relationship between the objective functions and the decision variables. This means that by choosing different values for the design variables, α_s and α_q, we can change the output in the objective functions CPU time, r_ε and r_u, during a msh free numerical analysis.

The initial population is 20 individuals, randomly generated. Then, the fitness function is evaluated for each individual and scaled using a rank process, to be later used in the selection process. The reproduction operator is implemented based on a tournament selection, with constraint dependent mutation and crossover. The optimization process is terminated if the number of generations exceeds 100, or if the average change in fitness function is less than 1×10^{-6}.

The results obtained for this first multi-objective optimization process are presented in Figure 26, for the first two objective functions, and Tables 1 to 3;

Table 1: The multi-objective Pareto front results for the regular nodal distribution of 52 nodes.

Index	CPU Time(s)	$\mathbf{r}_\varepsilon$	$\mathbf{r_u}$	$\alpha_\mathbf{s}$	$\alpha_\mathbf{q}$
1	0.2513	0.06615	0.06682	1.3628	0.4930
2	0.6347	1.413E-5	4.772E-4	3.9200	0.506
3	0.6437	7.194E-4	4.211E-4	3.7666	0.5109
4	0.2507	0.2327	0.2531	1.3818	0.5067

Table 2: The multi-objective Pareto front results for the regular nodal distribution of 165 nodes.

Index	CPU Time (s)	$\mathbf{r}_\varepsilon$	$\mathbf{r_u}$	$\alpha_\mathbf{s}$	$\alpha_\mathbf{q}$
1	3.7081	6.557E-5	2.009E-7	5.2789	0.5138
2	3.6090	1.336E-7	7.075E-5	5.2775	0.5137
3	3.6585	5.171E-5	1.552E-5	5.2788	0.5139

all the presented points are considered optimum from a computational point of view and non-dominated to each other, see Eberhart and Shi [2007]. For each point of the Pareto front, a couple of optimized parameters α_s and α_q are presented. As it can be seen, the optimization can lead to very accurate and convergent results. Moreover, the results show that α_s is constantly changing when different nodal distributions are considered, usually steadily increasing when more nodes are added to the model discretization, even though for α_q the best results are always obtained for values close to 0.5, regardless of the nodal distribution used.

This approach has one major drawback that is extremely high computational effort required, which could take hour, or days, depending on the number of nodes, even when running in parallel.

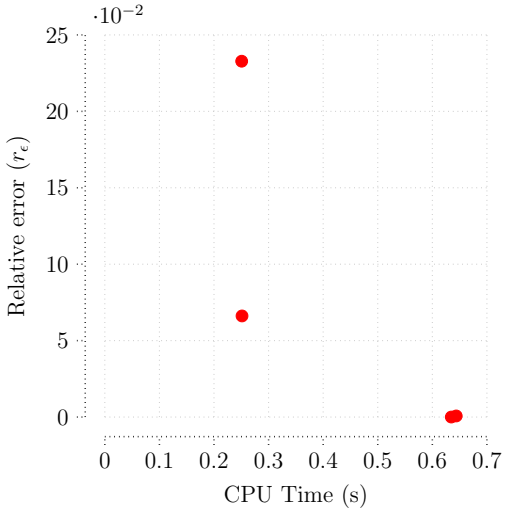

(a) Regular nodal distribution of 52 nodes.

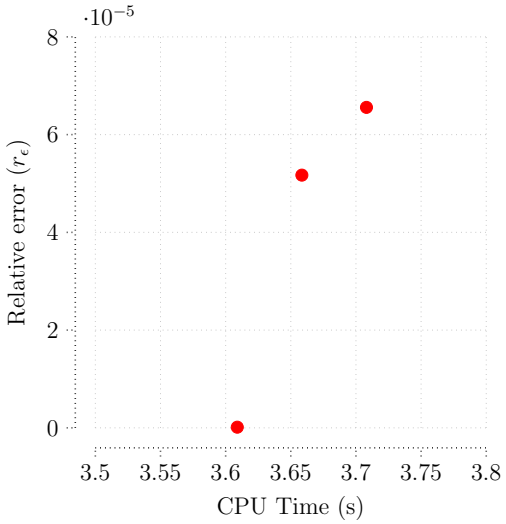

(b) Regular nodal distribution of 165 nodes.

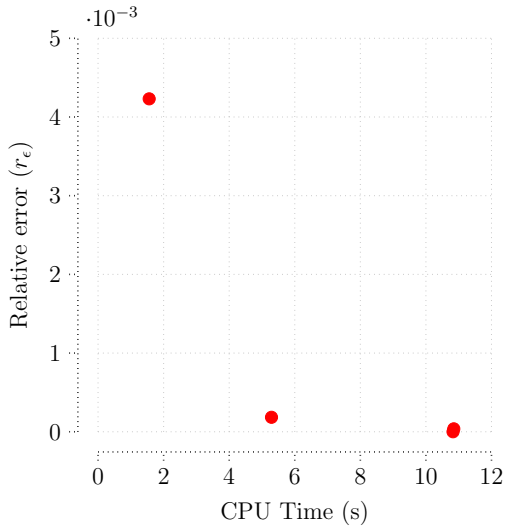

(c) Regular nodal distribution of 585 nodes.

Figure 26: The multi-objective Pareto front for regular nodal distributions of the beam discretization, considering CPU time, $\mathbf{r}_\varepsilon$ and $\mathbf{r}_\mathbf{u}$ as objective functions; only the first two are graphically presented.

Table 3: The multi-objective Pareto front results for the regular nodal distribution of 585 nodes.

Index	CPU Time (s)	$\mathbf{r}_\varepsilon$	$\mathbf{r_u}$	$\alpha_\mathbf{s}$	$\alpha_\mathbf{q}$
1	10.8267	6.190E-10	0.0001	7.2685	0.4971
2	5.2903	0.0002	1.314E-07	4.2103	0.4971
3	10.8503	3.733E-05	6.978E-05	7.2686	0.4973
4	1.5595	0.0042	0.0046	1.7677	0.4995

Another major drawback is analytical solution requirement, which is necessary to compute the relative error and is not available for more complex problems. Both drawbacks are unacceptable and require a more efficient approach, such as the one presented by the end of this section.

In the second optimization scheme, the compliance indicator, also known as flexibility indicator, derived from the local work theorem and computed only on the static boundary Γ_t, is chosen as objective function. CPU time is added as a objective function to control the analysis efficiency. Figures 27 to 29 demonstrate the behavior of the compliance indicator C and the relative energy

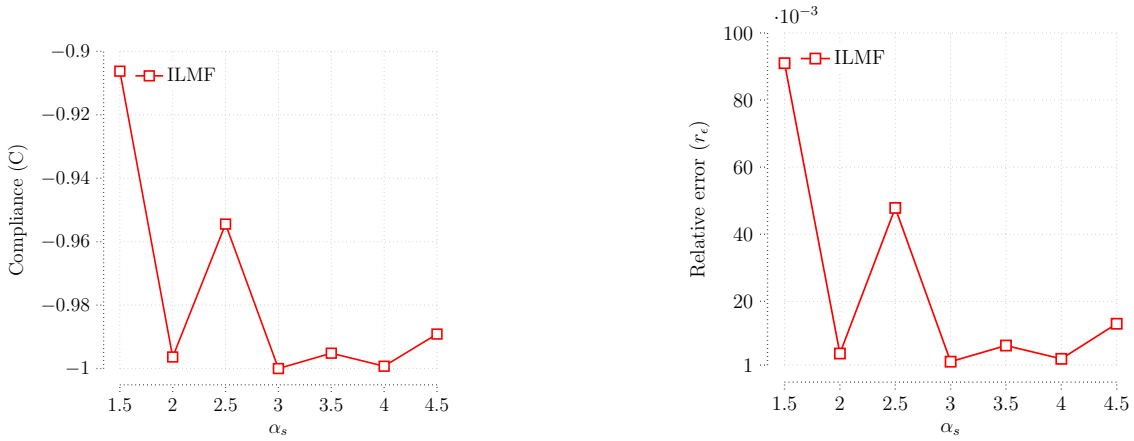

Figure 27: Compliance and relative error $\mathbf{r}_\varepsilon$ of the beam discretization with $13 \times 4 = 52$ nodes, as function of $\alpha_\mathbf{s}$ and for a fixed $\alpha_\mathbf{q} = 0.5$.

error r_ε, function of α_s and a fixed $\alpha_q = 0.5$. Both parameters showed to have a similar behavior, thus proving that C can be effectively used instead of r_ε. Furthermore, the computational effort required to perform the analysis is about 15 times faster for the compliance.

Consequently, for this second optimization approach, the GA is implemented in order to minimize the objective functions CPU time and the compliance indicator C. The decision variable α_s is defined as continuous in the interval

$$\alpha_s = [1.5 \ 10]. \tag{103}$$

The initial population is 20 individuals, randomly generated. Then, the fitness function is evaluated for each individual and scaled using a rank process, to be later used in the selection process. The reproduction operator is implemented based on a tournament selection, with constraint dependent mutation and crossover. The optimization process is terminated if the number of generations exceeds 100, or if the average change in fitness function is less than 1×10^{-6}.

The results obtained with the multi-objective optimization process are presented in Figure 26 and Tables 4 to 6, for a fixed $\alpha_q = 0.5$. From the results, it can be seen that all points in the Pareto front obtained a good accuracy, regardless of the nodal distribution. Once more, the convergence

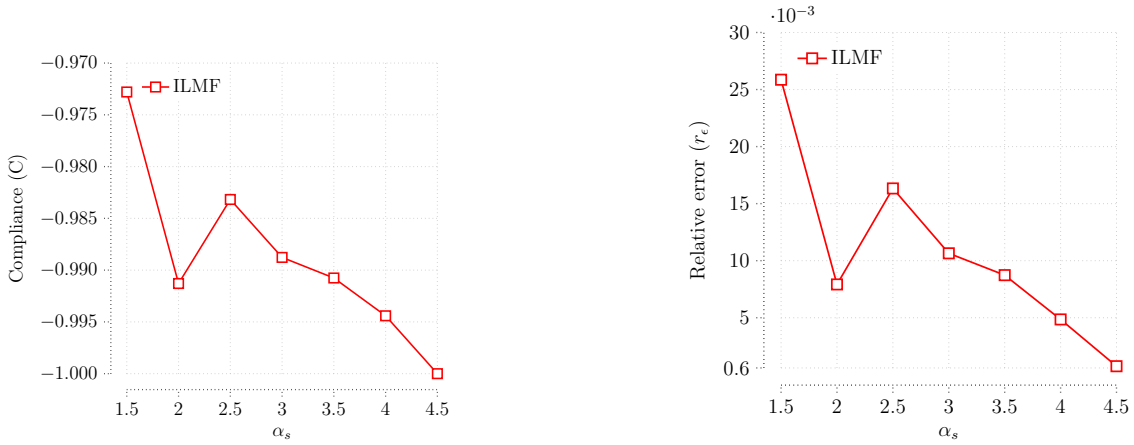

Figure 28: Compliance and relative error $\mathbf{r}_\varepsilon$ of the beam discretization with $\mathbf{33 \times 5 = 165}$ nodes, as function of $\alpha_\mathbf{s}$ and for a fixed $\alpha_\mathbf{q} = 0.5$.

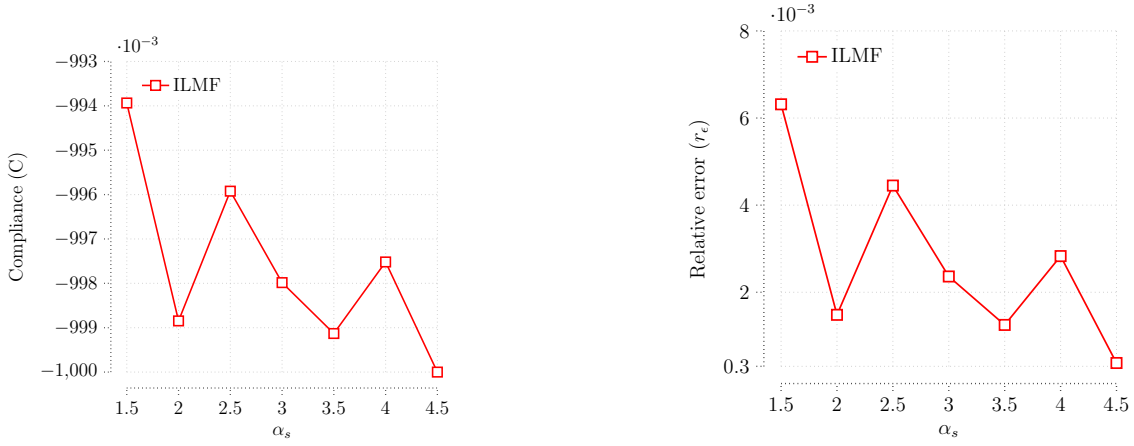

Figure 29: Compliance and relative error $\mathbf{r}_\varepsilon$ of the beam discretization with $\mathbf{65 \times 9 = 585}$ nodes, as function of $\alpha_\mathbf{s}$ and for a fixed $\alpha_\mathbf{q} = 0.5$.

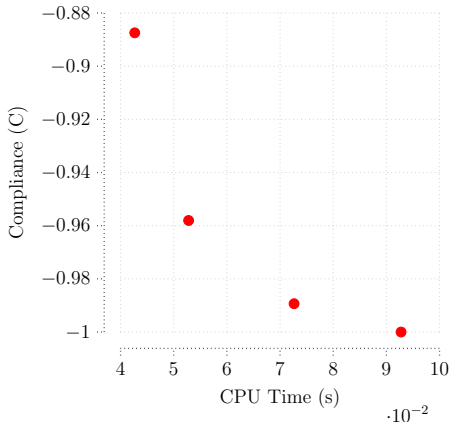

(a) Regular nodal distribution of 52 nodes.

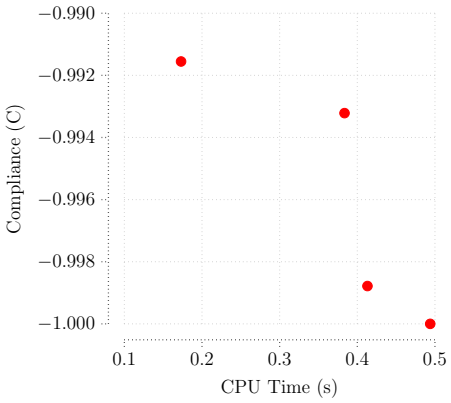

(b) Regular nodal distribution of 165 nodes.

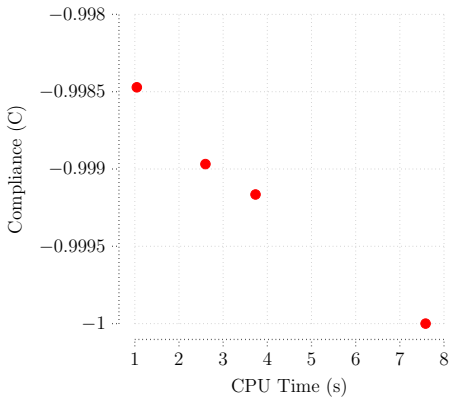

(c) Regular nodal distribution of 585 nodes.

Figure 30: The multi-objective Pareto front for regular nodal distributions of the beam discretization with $13 \times 4 = 52$, $33 \times 5 = 165$ and $65 \times 9 = 585$ nodes, considering CPU time and compliance indicator as objective functions; for a fixed $\alpha_{\mathbf{q}} = 0.5$.

Table 4: The multi-objective Pareto front results for the regular nodal distribution of 52 nodes and a fixed $\alpha_{\mathbf{q}} = 0.5$

Index	CPU Time (s)	Compliance	$\mathbf{r}_{\varepsilon}$	$\mathbf{r}_{\mathbf{u}}$	$\alpha_{\mathbf{s}}$
1	0.0427	-0.887	0.0993	0.1069	1.3585
2	0.0923	-1	0.0051	0.0042	3.1515
3	0.0726	-0.989	0.0044	0.0067	2.0053
4	0.0528	-0.958	0.0346	0.0373	1.7414

Table 5: The multi-objective Pareto front results for the regular nodal distribution of 165 nodes and a fixed $\alpha_{\mathbf{q}} = 0.5$

Index	CPU Time (s)	Compliance	$\mathbf{r}_{\varepsilon}$	$\mathbf{r}_{\mathbf{u}}$	$\alpha_{\mathbf{s}}$
1	0.4131	-0.9987	6.660E-04	5.510E-04	4.4932
2	0.4940	-1	0.0019	0.0017	4.7085
3	0.1730	-0.9915	0.0064	0.0066	1.8935
4	0.3835	-0.9932	0.0049	0.0050	3.9966

Table 6: The multi-objective Pareto front results for the regular nodal distribution of 585 nodes and a fixed $\alpha_{\mathbf{q}} = 0.5$

Index	CPU Time (s)	Compliance	$\mathbf{r}_{\varepsilon}$	$\mathbf{r}_{\mathbf{u}}$	$\alpha_{\mathbf{s}}$
1	2.5991	-0.9989	4.022E-04	3.821E-04	4.4965
2	3.7328	-0.9991	2.040E-04	1.883E-04	4.5330
3	1.0455	-0.9984	8.209E-04	8.768E-04	1.8733
4	7.5833	-1	6.614E-04	6.352E-04	9.6232

is guaranteed, meaning that an increase in the overall number of nodes of the nodal distribution also increases the overall accuracy. Although the lowest relative error is not always obtained with the lowest compliance indicator, this is barely a problem since the local Pareto-optimal is always close to the global Pareto-optimal, leading to very good results for all points. The aforementioned reduced computational effort is also present in this analysis, as expected, performing computations in minutes instead of hours.

For a complete optimization of mesh free parameters, α_q also need to be addressed. The shortest and most convenient approach is to guarantee that the total area of the local weak form domain is as similar as possible to the overall area of the whole body domain. Hence, the output area of the local domain, equation (49), is chosen as an objective function for this optimization. For the sake of simplicity, a single-objective optimization is performed. If a problem has N nodes in total, the design variable α_q is a vector containing N components defined as continuous in the interval

$$\alpha_q = [0.495 \;\; 0.95]\,, \tag{104}$$

to ensure the locality of the MLS approximation and that the local sub-domains of the internal nodes are entirely within the solution domain, without being intersected by the global boundary.

The initial population is 200 individuals, randomly generated. Also, random populations from previous analysis within the optimization process are introduced randomly to increase the computational efficiency. Then, the fitness function is evaluated for each individual and scaled using a rank process, to be later used in the selection process. The reproduction operator is implemented based on a stochastic uniform selection, with constraint dependent mutation and crossover. The optimization process is terminated if the number of generations exceeds predefined values, or if the average change in fitness function is less than 1×10^{-6}.

Figure 31 presented the results of the single-objective optimization, as function of different

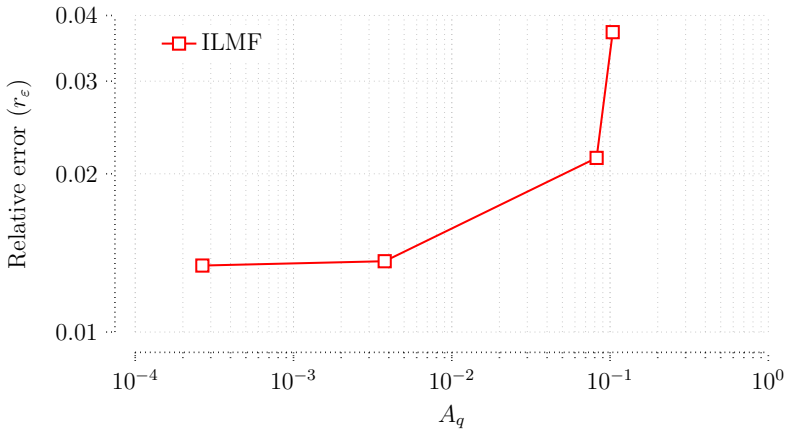

Figure 31: Relative energy error of ILMF as function of the local sub-domain of integration area $\mathbf{A_q}$, for the regular nodal distribution of 165 nodes.

predefined maximum number of generations in the algorithm stopping criteria, considering 100, 200, 400 and 800 generations, for a fixed $\alpha_s = 4.5$. The accuracy gradually improves as A_q converge to the area of the posed problem.

Note that the computational effort of this analysis is also very low, thus leading to fast results. This is mostly due to the introduction of random populations from previous analysis. The first analysis, preferably from a smaller nodal distribution, can be performed really fast and the population used saved in MATLAB internal memory. Later, now for a greater nodal distributions, the optimization will run faster since it will use random feasible results from the previous analysis, accelerating the whole process.

Lastly, this final optimization approach combines the features of the previous optimization schemes into a single fully automated routine to compute ILMF discretization parameters α_s and α_q, preserving the presented effectiveness.

This last optimization is divided in two steps. First, α_q is optimized using A_q as objective function. The output of this process is a vector containing one value of α_q for each node in the nodal distribution. Second, α_s is optimized using compliance C and CPU time as objective functions, considering the results obtained in the previous optimization.

The results obtained from the automated multi-objective optimization are presented in Figure 32 and Tables 7 to 9, in which all of the presented points in the Pareto front are feasible,

Table 7: Pareto front of the multi-objective optimization for the regular nodal distribution of 52 nodes using the automatic parameters optimization routine.

Index	CPU Time (s)	Compliance	$\mathbf{r}_\varepsilon$	$\mathbf{r_u}$	$\alpha_\mathbf{s}$
1	0.0495	-0.942	0.0495	0.0522	1.6919
2	0.0773	-0.990	0.0046	0.0051	2.9747
3	0.0821	-1	0.0052	0.0043	3.1443
4	0.0649	-0.984	0.0091	0.0117	1.9415
5	0.0507	-0.959	0.0091	0.0117	1.7464

non-dominated and optimum, from a computational perspective. The results are a clear evidence of the accuracy and efficiency of the automated routine, effectively combining the aforementioned features into a single process.

In order to present the efficiency of the optimization process, regardless of the optimization technique, GA and SOS algorithms are compared. Thus, similar settings and stopping criteria

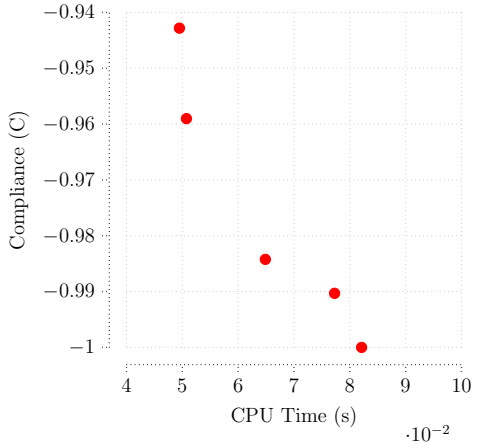

(a) Regular nodal distribution of 52 nodes.

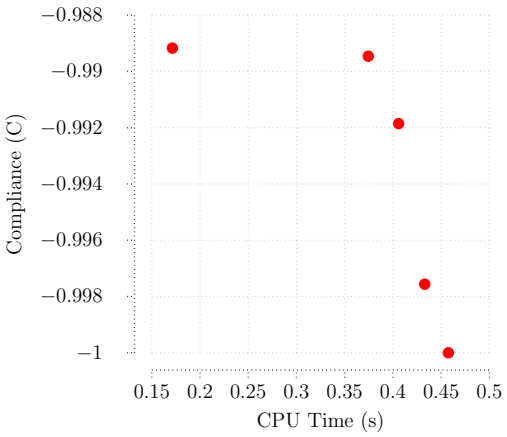

(b) Regular nodal distribution of 165 nodes.

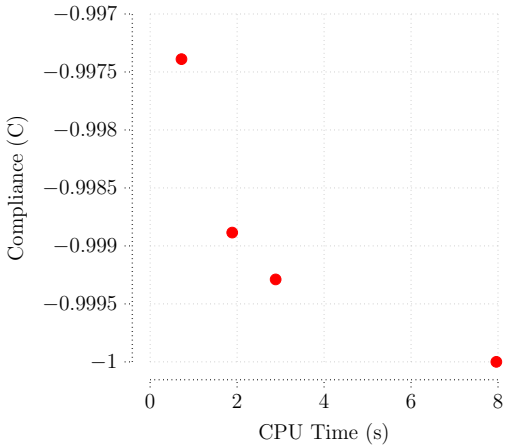

(c) Regular nodal distribution of 585 nodes.

Figure 32: The multi-objective Pareto front for regular nodal distributions of the beam discretization with the automatic parameters optimization routine.

Table 8: Pareto front of the multi-objective optimization for the regular nodal distribution of 165 nodes using the automatic parameters optimization routine.

Index	CPU Time (s)	Compliance	$\mathbf{r}_\varepsilon$	$\mathbf{r_u}$	$\alpha_\mathbf{s}$
1	0.3744	-0.9894	0.0083	0.0083	3.8145
2	0.4575	-1	0.0023	0.0022	4.6639
3	0.1713	-0.9891	0.0084	0.0087	1.9470
4	0.4330	-0.9975	1.281E-04	1.980E-04	4.3474
5	0.4059	-0.9918	0.0059	0.0059	3.9606

Table 9: Pareto front of the multi-objective optimization for the regular nodal distribution of 585 nodes using the automatic parameters optimization routine.

Index	CPU Time (s)	Compliance	$\mathbf{r}_\varepsilon$	$\mathbf{r_u}$	$\alpha_\mathbf{s}$
1	0.7201	-0.997	0.0016	9.535E-04	1.5
2	2.8858	-0.999	1.660E-04	2.557E-04	4.5010
3	1.8870	-0.998	2.463E-04	6.637E-05	3.4838
4	7.9617	-1	9.110E-04	9.074E-04	9.5744

were defined for both of them. Because SOS is a parameter-free optimization method, only the population size and the maximum number of function evaluations were defined, for this case as 20 and 100, respectively. Both algorithms stop if the average change in fitness function is less than 1×10^{-6} or the maximum number of function evaluations or generations is reached.

The compliance C is chosen as the objective function, for a fixed scalar $\alpha_q = 0.5$. The decision variable α_s is defined as continuous in the interval

$$\alpha_s = [1.5 \ 10]. \tag{105}$$

The comparison is presented in Figure 33, based on the number of generations or function it-

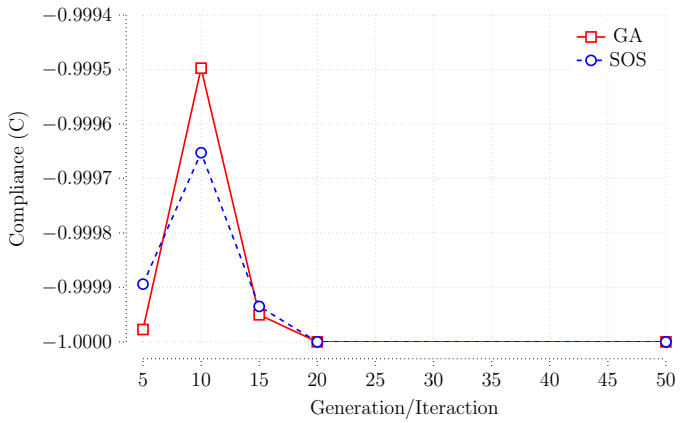

Figure 33: Comparison between GA and SOS relative to the maximum number of generations/iterations.

erations, and Table 10, where the optimization efficiency of both techniques can be seen. Note that GA is slightly less efficient than SOS. Nevertheless, the values of α_s obtained on both approaches are very similar, close to the ones previously obtained and therefore leading to very accurate results. SOS as a computational cost higher than GA due to the efficiency of the genetic operators that are refined for this type of problem.

Table 10: The comparative analysis of GA and SOS, for a single-objective optimization of the cantilever beam. C and OCE stands for structural compliance and optimization computational effort, respectively.

	SOS			GA		
Nodes	**C**	**OCE (s)**	$\alpha_{\mathbf{s}}$	**C**	**OCE (s)**	$\alpha_{\mathbf{s}}$
52	-0.999993	7.05	3.156	-1	5.94	3.151
165	-0.981476	52.28	4.705	-0.981477	26.48	4.708
585	-0.962864	144.40	9.631	-0.962865	127.70	9.623

The simplicity is a key advantage provided by the SOS optimization, which requires only 2 parameters to be set, in contrast to the GA optimization that requires a lot more parameters. Even though SOS is a very promising optimization algorithm, there is a set of libraries and optimization option on MATLAB environment for GA that are not yet available for SOS.

8.2 Benchmark Problem 2 – Plate with a Circular Hole

On this example, an infinite plate with a centered circular hole under unidirectional unit tension along the x_1 direction is analyzed, as portrait in Figure 34. The symmetry of the problem about

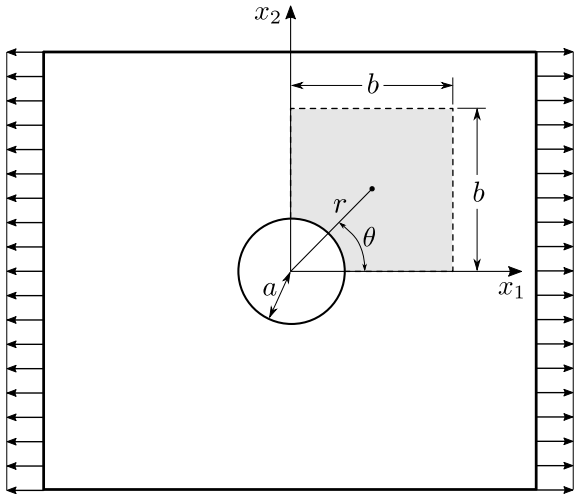

Figure 34: Plate with a hole.

the horizontal and the vertical axes allow the use of only a portion of the upper right quadrant of the plate. The section has dimensions $b \times b$ and the center circle has a radius $a = 1$, with $b = 5a$.

The analytical stress distribution in the plate is

$$\begin{aligned}
\sigma_{11}(r,\theta) &= 1 - \frac{a^2}{r^2}\left(\frac{3}{2}\cos 2\theta + \cos 4\theta\right) + \frac{3}{2}\frac{a^4}{r^4}\cos 4\theta \\
\sigma_{22}(r,\theta) &= -\frac{a^2}{r^2}\left(\frac{1}{2}\cos 2\theta - \cos 4\theta\right) - \frac{3}{2}\frac{a^4}{r^4}\cos 4\theta \\
\sigma_{12}(r,\theta) &= -\frac{a^2}{r^2}\left(\frac{1}{2}\sin 2\theta + \sin 4\theta\right) + \frac{3}{2}\frac{a^4}{r^4}\sin 4\theta,
\end{aligned} \tag{106}$$

where r and θ are the usual polar coordinates, centered at the center of the hole. A plane-stress

state is considered, which leads to displacements

$$\begin{aligned} u_1(r,\theta) &= -\frac{\cos\theta}{2r^3E}\left[4a^4\cos^2\theta\,(1+\nu)\left(1-r^2\right) - 3a^4(1+\nu) + (ar)^2(1-3\nu) - 2r^4\right] \\ u_2(r,\theta) &= -\frac{\sin\theta}{2r^3E}\left[4a^4\cos^2\theta\,(1+\nu)\left(1-r^2\right) - a^4(1+\nu) + (ar)^2(\nu-3) + 2r^4\nu\right]. \end{aligned} \tag{107}$$

In the bottom and left edges of the plate are defined as kinematic boundaries, with displacements $u_2(x_1, x_2 = 0)$ specified on the bottom and $(u_1(x_1 = 0, x_1 = L, x_2) = 0)$ specified on the left edges. For the right and top edges, static boundaries are assumed, with tractions computed from the stresses of the analytical solution (106) applied as $t_j = \sigma_{ij}n_i$, in which n_i represents the components of the unit outward normal to the edge of the plate. Young′s modulus $E = 1.0 \times 10^5$ and the Poisson′s ratio $\nu = 0.25$ are considered.

In order to solve this plate, discretization with 9 nodes in the tangential direction and 15 nodes in the radial direction, distributed as shown in Figure 35, with circular local domains and second

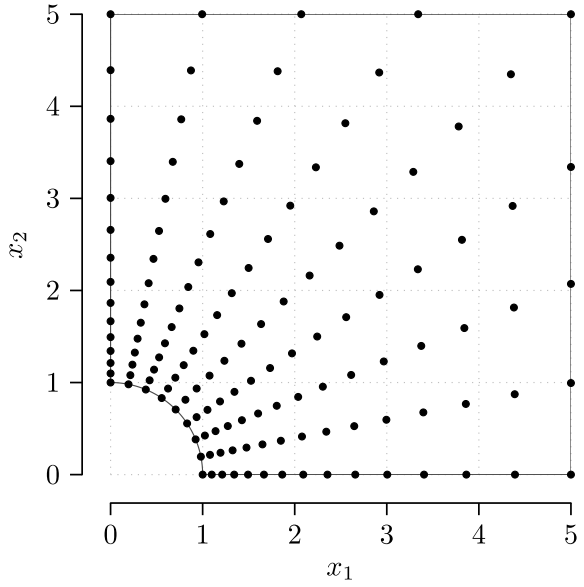

Figure 35: Discretization of the plate with a hole.

order polynomial basis for the MLS approximation. ILMF integration was performed with 1 point at the boundary of each quadrant of the circular integration domain, as schematically represented in Figure 7.

The computed displacements are shown in Figure 36, where it can be seen a very good agreement with the results of the analytical solution. The stresses at nodes also provided very good outputs when compared to the exact solution, as shown in Figure 37.

Relative errors of $r_u = 9.2 \times 10^{-3}$ and $r_\epsilon = 4.1 \times 10^{-3}$ were obtained for this simple discretization, which highlight the versatility of ILMF.

8.3 Benchmark Problem 3 – Edge-Cracked Plate

This benchmark problem presents the direct evaluation of SIF, through the SST implemented in the ILMF model, an efficient and accurate tool for the analysis of cracked plates. For this analysis, two problems of edge-cracked square plates, respectively under mode-I and mode-II loadings are presented; and a third case of a square plate with an edge slant crack, under mixed-mode deformation, is also presented.

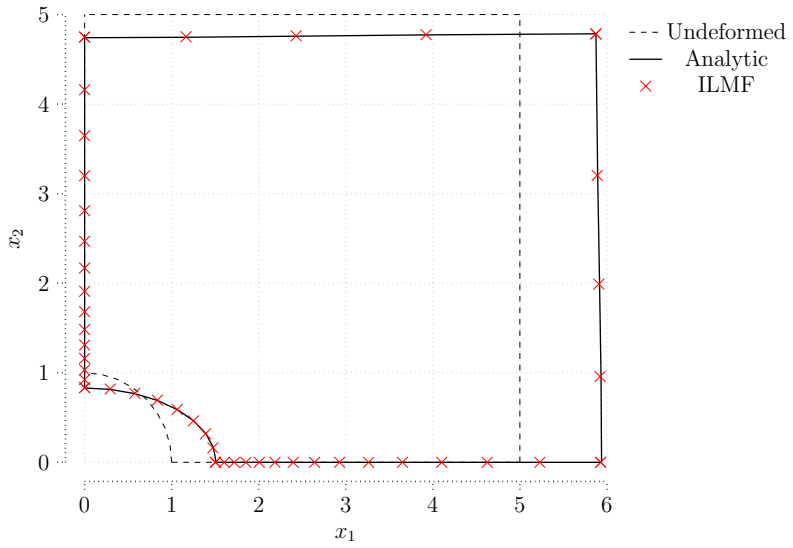

Figure 36: Boundary displacements of the plate with a hole.

The presence of the crack in a mesh free model requires a special treatment of the non-convex domain resulting from the crack discontinuity. Crack faces are modeled with two sets of overlapping nodes, in a way that the nodes of each line have influence only in the respective side, shared by a single crack tip with influence in both sides of the crack. For each node within the crack, the visibility criterion is used to define the compact support, as represented in Figure 38. Therefore, for nodes within the crack faces, the compact support and the local integration domain are defined as in the case of a traction-free boundary node. However, for the crack tip node, the compact support is defined as in the case of an interior node, while for the local integration domain the size as half of the case of the interior nodes.

Matrices g and f, containing the William's singular solution at each crack tip, equations (71) and (72) respectively, are computed with 3 Gauss quadrature points.

The DBEM with the J-integral (J-DBEM), presented by Portela and Aliabadi [1993], is used to compare the results obtained with ILMF formulation. The DBEM modeling strategy considers piecewise-straight cracks that are discretized with straight discontinuous quadratic boundary elements. Continuous quadratic boundary elements are used along the remaining boundaries of the problem, except at the intersection between a crack and an edge, where semi-discontinuous boundary elements are used on the edge. Self-point discontinuous boundary elements are integrated analytically, while Gaussian quadrature, with sub-element integration, is carried out for the remaining integrations.

In the ILMF numerical model, rectangular local domains of integration, with discretization parameters $\alpha_s = 1.5 \sim 3$ and $\alpha_q = 0.5$ are considered. The MLS approximation with first-order polynomial basis and quartic spline weighting function are also considered.

8.3.1 Mode-I Loading

First, a square edge-cracked plate, represented in Figure 39, is considered for the analysis, in which a denote the length of the crack, w the width of the plate and the height by $h = w/2$. The uniform traction $\bar{\mathbf{t}} = \sigma$ is applied at the plate, symmetrically at the ends. In order to compare the ILMF accuracy with the highly accurate values reported by Civelek and Erdogan [1982], $h/w = 0.5$ is considered on this problem. Five cases are presented, for $a/w = 0.2, 0.3, 0.4, 0.5$ and 0.6. The nodal distribution used in the analysis is represented in Figure 40, with a regular nodal distribution

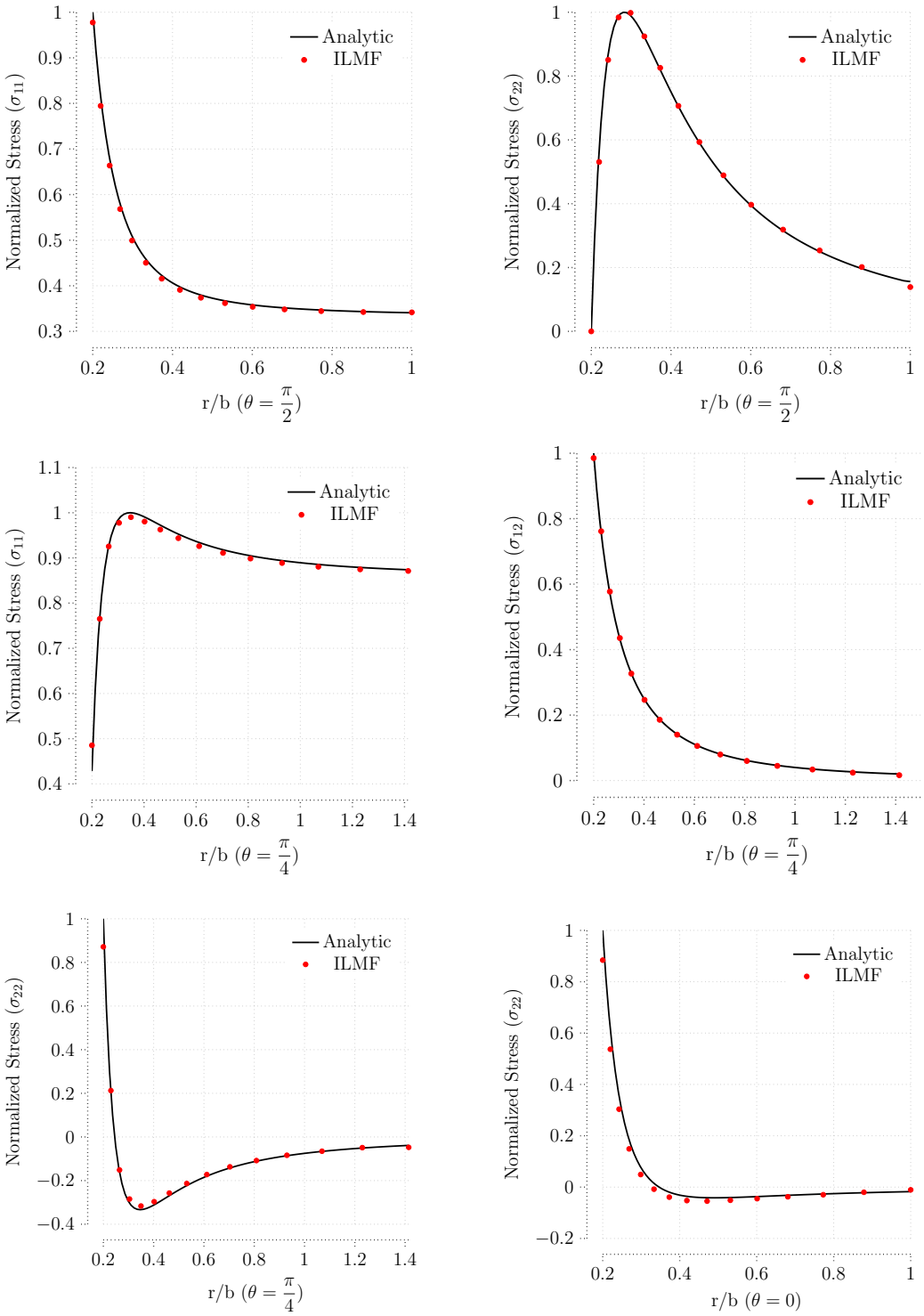

Figure 37: Stress distribution of the plate with circular hole for $\theta = 0, \frac{\pi}{4}, \frac{\pi}{2}$

.

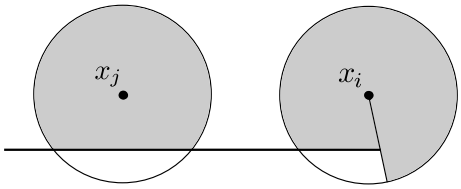

Figure 38: The visibility criterion, originally introduced by Belytschko et al. [1994a].

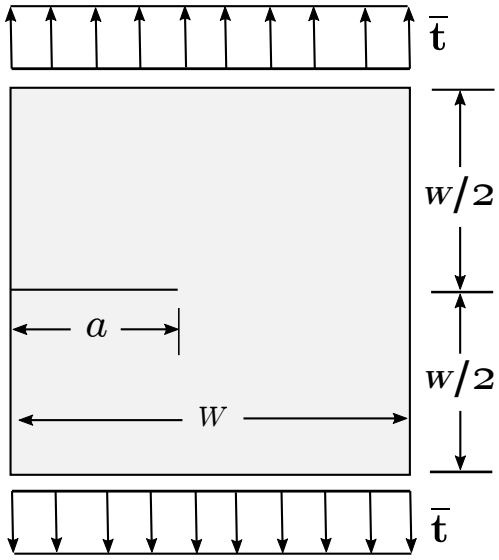

Figure 39: Square plate with a single edge crack under mode-I loading $(\mathbf{h}/\mathbf{w} = 0.5)$.

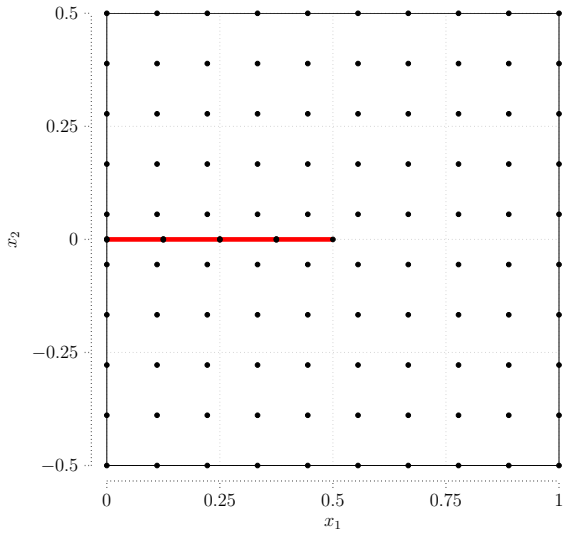

Figure 40: Discretization of the plate with a regular nodal distribution, for $\mathbf{a}/\mathbf{w} = 0.5$. The red line represents the crack faces.

of $10 \times 10 = 100$ nodes, with additional overlapping nodes on the crack faces. For all the five cases of crack length, only the nodal distribution of the crack faces was modified, adding more nodes for longer lengths, always without any refinement of the discretization around the crack tip.

Results obtained are presented in Table 11, where ILMF correspond the values obtained in this

Table 11: Square plate with a single edge crack under mode-I loading.

	$\mathbf{K_I/(\bar{t}\sqrt{\pi a})}$			**% Error**	
a/w	**ILMF**	**J-DBEM**	**Reference**	**ILMF**	**J-DBEM**
0.2	1.520	1.495	1.488	0.0216	0.005
0.3	1.967	1.858	1.848	0.0647	0.005
0.4	2.413	2.338	2.324	0.0387	0.006
0.5	2.973	3.028	3.010	0.0122	0.006
0.6	3.991	4.184	4.152	0.0387	0.008

analysis, J-DBEM represents the values obtained with the J-integral implemented in the DBEM, published by Portela and Aliabadi [1993], and reference represent the values published by Civelek and Erdogan [1982]. Percentage errors are calculated from the values of reference. The results clearly show that ILMF have a good agreement with J-DBEM and the reference values. Since this is a mode-I loading crack problem, the SIF values of the mode-II are always below 10^{-7}. The plate deformed configuration is schematically represented in Figure 41.

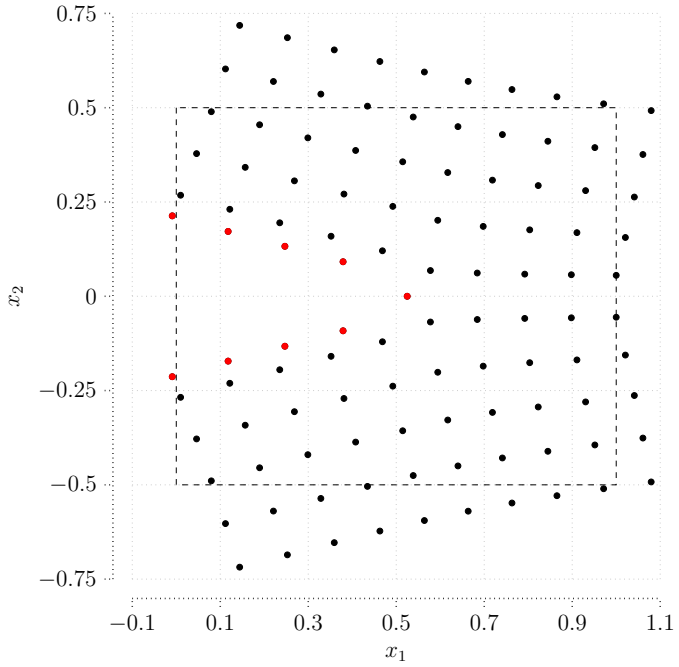

Figure 41: Deformed configuration of the plate, for $\mathbf{a/w = 0.5}$, under mode-I loading.

8.3.2 Mode-II Loading

Now, consider a square edge-cracked plate, as presented in Figure 42. The crack length is denoted by a and $h/w = 0.5$ is considered. The uniform traction $\bar{\mathbf{t}}$ is applied anti-symmetrically at the plate sides, parallel to the crack. This is a very complex and difficult problem, for which there are

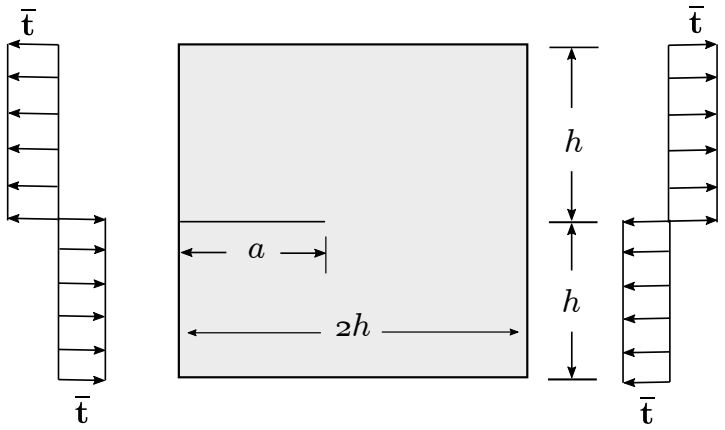

Figure 42: Square plate with a single edge crack under mode-II loading ($\mathrm{w} = 2\mathrm{h}$).

no published benchmark results. Hence, the results provided by J-DBEM are used as reference for this problem. Five cases are presented, for $a/w = 0.2, 0.3, 0.4, 0.5$ and 0.6. The nodal distribution used in the analysis is represented in Figure 43, with a regular nodal distribution of $16 \times 16 = 256$

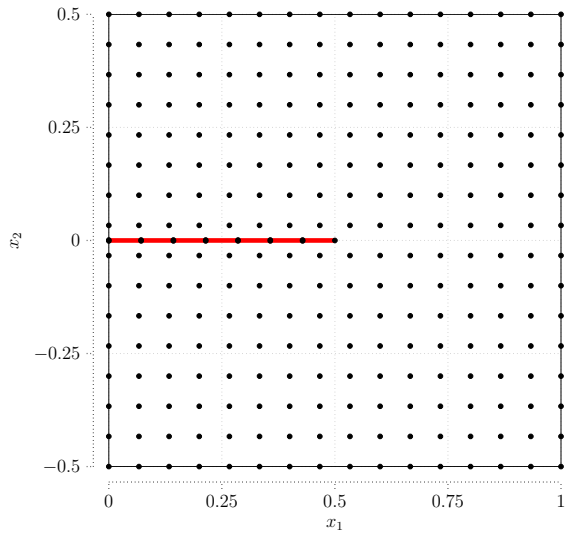

Figure 43: Discretization of the plate with a regular nodal distribution, for $\mathrm{a}/\mathrm{w} = 0.5$. The red line represents the crack faces.

nodes, with additional overlapping nodes on the crack faces. For all the five cases of crack length, only the nodal distribution of the crack faces was modified, adding more nodes for longer lengths, always without any refinement of the discretization around the crack tip.

Results obtained are presented in Table 12, where percentage errors are calculated from the values of J-DBEM. For this problem, the SIF values obtained for the mode-I are always below 10^{-3}, since this is a typical mode-II crack problem. Figure 44 shows the deformed configuration of the plate.

Table 12: Square plate with a single edge crack under mode-II loading.

$\mathbf{a/w}$	$\mathbf{K_{II}/(\bar{t}\sqrt{\pi a})}$		
	ILMF	**J-DBEM**	**% Error**
0.2	0.416	0.435	0.0436
0.3	0.338	0.358	0.0532
0.4	0.296	0.304	0.0261
0.5	0.248	0.262	0.0522
0.6	0.218	0.223	0.0218

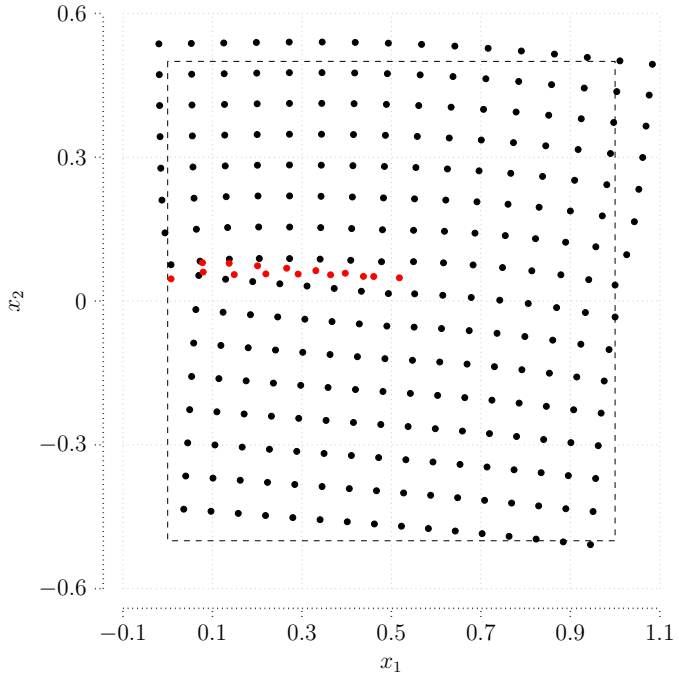

Figure 44: Deformed configuration of the plate, for $\mathbf{a/w = 0.5}$, under mode-II loading.

8.3.3 Mixed-Mode Loading

Consider now a plate with an edge slant crack, as showed in Figure 45, in mixed-mode deformation derived from a remote stress σ. Three cases are presented, for $a/w = 0.2, 0.4$ and 0.6 with $\alpha = 30^o$; and two cases, for $a/w = 0.2$ and 0.4 with $\alpha = 60^o$. This problem was analyzed with the nodal distribution represented in Figure 46; with a regular nodal distribution of $16 \times 16 = 256$ nodes, with additional overlapping nodes on the crack faces. For all cases of crack length, only the nodal distribution of the crack faces was modified, adding more nodes for longer lengths, always without any refinement of the discretization around the crack tip.

Tables 13 and 14 show, respectively, the values of $K_I/(\sigma\sqrt{\pi a})$ and $K_{II}/(\sigma\sqrt{\pi a})$, as well as the percentage relative to the difference between the appropriate values published by Murakami [1987b], used as reference, and ILMF results; as a function of a/W and for $\alpha = 30^o$. Tables 15 and 16 present the values of $K_I/(\sigma\sqrt{\pi a})$, $K_{II}/(\sigma\sqrt{\pi a})$ and the percentage relative to the difference between the appropriate values published by Murakami [1987b] and ILMF; as a function of a/W, for $\alpha = 60^o$. Once more, the results obtained for this problem are in agreement with those obtained with the J-DBEM and those published in references, provided by Murakami [1987b] and Tada [2000]. It is important to remark the high level of accuracy obtained in all cracked plate problems, always considering coarseness nodal distributions, without any refinement around the

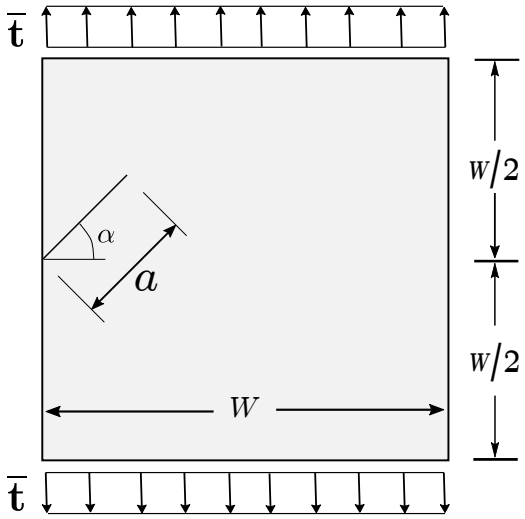

Figure 45: Square plate with an edge slant crack, under remote stress σ loading.

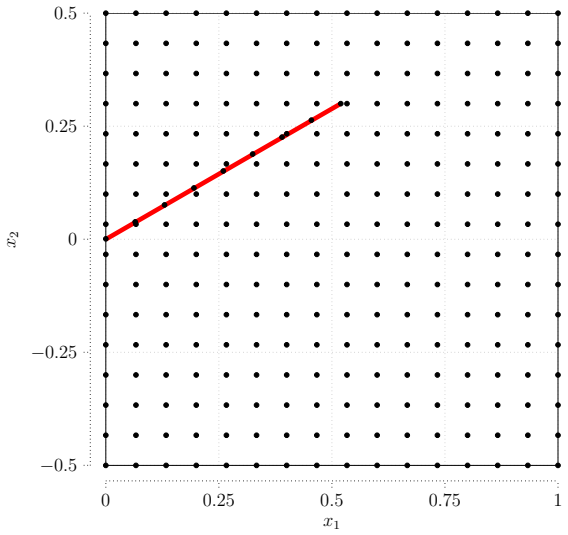

Figure 46: Discretization of the plate with a regular nodal distribution, for $\mathbf{a/w = 0.5}$. The red line represents the crack faces.

Table 13: Stress intensity factor $\mathbf{K_I/(\sigma\sqrt{\pi a})}$ for the edge slant crack $(\alpha = 30^o)$.

	$\mathbf{K_I/(\sigma\sqrt{\pi a})}$			% Difference	
a/W	**ILMF**	**J-DBEM**	**Reference**	**ILMF**	**J-DBEM**
0.2	1.164	1.082	1.100	0.058	0.016
0.4	1.513	1.545	1.550	0.024	0.003
0.6	2.732	2.572	2.550	0.071	0.009

crack tip.

The deformed configuration of the plate is show in Figure 47.

Table 14: Stress intensity factor $\mathbf{K_{II}}/(\sigma\sqrt{\pi \mathrm{a}})$ for the edge slant crack $(\alpha = 30^{\mathrm{o}})$.

	$\mathbf{K_{II}}/(\sigma\sqrt{\pi \mathrm{a}})$			% Difference	
a/W	ILMF	J-DBEM	Reference	ILMF	J-DBEM
0.2	0.325	0.351	0.350	0.071	0.003
0.4	0.471	0.474	0.470	0.002	0.009
0.6	0.580	0.700	0.700	0.171	0.000

Table 15: Stress intensity factor $\mathbf{K_{I}}/(\sigma\sqrt{\pi \mathrm{a}})$ for the edge slant crack $(\alpha = 60^{\mathrm{o}})$.

	$\mathbf{K_{I}}/(\sigma\sqrt{\pi \mathrm{a}})$			% Difference	
a/W	ILMF	J-DBEM	Reference	ILMF	J-DBEM
0.2	0.543	0.495	0.500	0.086	0.010
0.4	0.603	0.592	0.600	0.055	0.013

Table 16: Stress intensity factor $\mathbf{K_{II}}/(\sigma\sqrt{\pi \mathrm{a}})$ for the edge slant crack $(\alpha = 60^{\mathrm{o}})$.

	$\mathbf{K_{II}}/(\sigma\sqrt{\pi \mathrm{a}})$			% Difference	
a/W	ILMF	J-DBEM	Reference	ILMF	J-DBEM
0.2	0.327	0.356	0.360	0.092	0.011
0.4	0.439	0.413	0.420	0.045	0.017

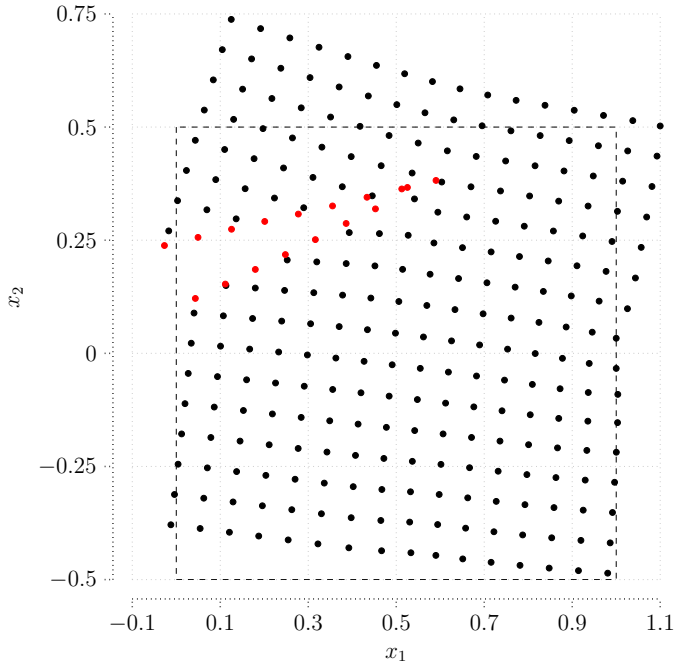

Figure 47: Deformed configuration of the plate, for $\mathrm{a/w} = 0.5$, under mixed-mode loading.

8.4 Benchmark Problem 4 – Central Cracked Plate

For practical applications, albeit curved in most cases, can be effectively modeled as piece-wise flat, when the path of a crack is concerned. As reported by Caicedo and Portela [2015], the Williams' fields can be locally used at each crack tip, as a particular solution of an arbitrary piece-wise flat crack. Hence, to deal with several cracks simultaneously, superposition is used in SST strategy in a way that, in the proximity of each crack tip, the Williams' field is locally used in the

regularization procedure. As a direct consequence, the central cracked plate can be considered as a multi-cracked plate, with two distinct crack tips.

Consider a rectangular plate with a central slant crack, as show in Figure 48. The uniform

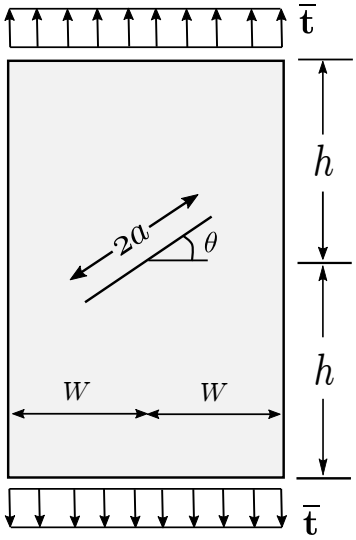

Figure 48: Rectangular plate with a central slant crack, under uniform traction.

traction $\bar{\mathbf{t}}$ is applied symmetrically at the ends. The ratio between the height and the width of the plate is given by $h/w = 2$. The crack length is $2a$ and form an angle of $\theta = 45^o$ with the horizontal direction. The results published by Murakami [1987a] are used as reference. Three cases are presented, for $a/w = 0.2, 0.4$ and 0.6. For this particular case, discretization parameters were considered as $\alpha_s = 5 \sim 8$ and $\alpha_q = 0.5$. The discretization was performed with the nodal distribution, as show in Figure 49; with a regular nodal distribution of $7 \times 12 = 84$ nodes, with additional overlapping nodes on the crack faces. For all three cases of crack length, only the nodal distribution of the crack faces was modified, adding more nodes for longer lengths, always without any refinement of the discretization around the crack tip.

Tables 17 and 18 demonstrate the results obtained, for the values of $K_I/(\bar{t}\sqrt{\pi a})$ and $K_{II}/(\bar{t}\sqrt{\pi a})$, as well as comparisons with the appropriate values of the reference presented by Murakami [1987a], as a function of a/W. The results obtained clearly demonstrate the excellent accuracy

Table 17: Stress intensity factor $\mathbf{K_I/(\bar{t}\sqrt{\pi a})}$ for the central slant crack $(\theta = \mathbf{45^o})$.

	$\mathbf{K_I/(\bar{t}\sqrt{\pi a})}$			% Difference	
a/W	**ILMF**	**J-DBEM**	**Reference**	**ILMF**	**J-DBEM**
0.2	0.519	0.521	0.518	0.002	0.006
0.4	0.575	0.576	0.572	0.005	0.007
0.6	0.626	0.666	0.661	0.053	0.001

of this new formulation of the ILMF numerical model that is an efficient tool for the mixed-mode deformation analysis of cracked plates.

The deformed configuration of the plate is presented in Figure 50.

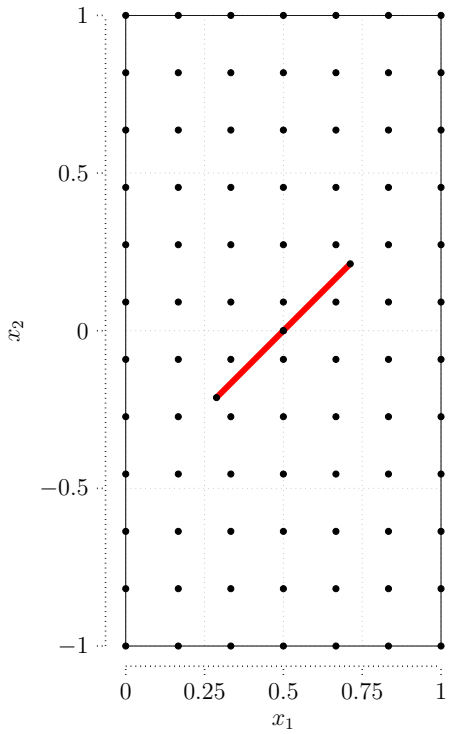

Figure 49: Discretization of the plate with a regular nodal distribution for $\mathrm{a/w} = 0.6$. The red line represents the crack faces.

Table 18: Stress intensity factor $\mathrm{K_{II}}/(\bar{\mathrm{t}}\sqrt{\pi \mathrm{a}})$ for the edge slant crack $(\theta = 45^{\mathrm{o}})$.

	$\mathrm{K_{II}}/(\bar{\mathrm{t}}\sqrt{\pi \mathrm{a}})$			% Difference	
a/W	ILMF	J-DBEM	Reference	ILMF	J-DBEM
0.2	0.529	0.508	0.507	0.043	0.002
0.4	0.532	0.529	0.529	0.005	0.001
0.6	0.585	0.569	0.567	0.032	0.003

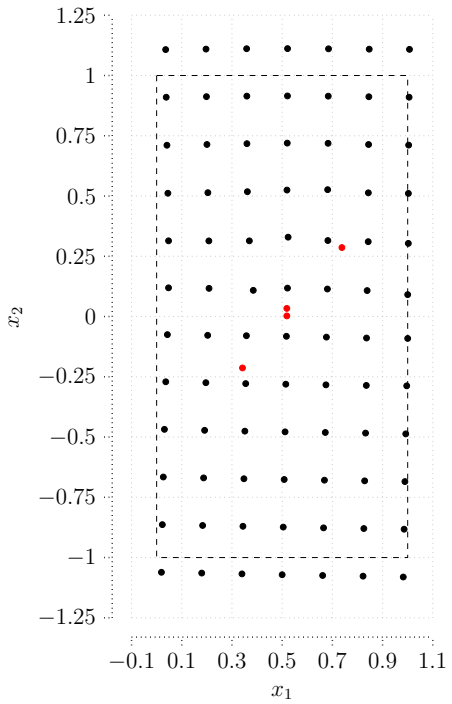

Figure 50: Deformed configuration of the plate for $\mathrm{a/w} = 0.6$ under uniform traction.

9 Concluding Remarks

The local mesh free method for solving linear elastic and fracture mechanics problems were presented on this chapter. The method is derived from the work theorem, where the formulation leads to a weak form of the weighted residual statement of a statically admissible stress field, kinematically formulated with a rigid-body displacement. The node-by-node discretization considers the MLS approximation and implements a reduced numerical integration.

In a nodal discretization, the size of the compact support and the size of the local integration domain of each node are parameters directly linked to the accuracy and efficiency of local mesh free methods. In this paper, both discretization parameters are automatically defined through a multi-objective optimization process based on genetic algorithms and symbiotic organism search algorithm.

Benchmark test problems were analyzed in order to assess the accuracy and efficiency of the local mesh free method. Both regular and irregular nodal distributions can be considered. For irregular nodal distributions, the combination of stable results and a high accuracy are obtained, even for severe irregular distributions. The optimization scheme defined on this chapter is very efficient, from a computational point of view, and do not require any analytical solution to be performed. Therefore, the local mesh free method proved to be a reliable and robust formulation for solving linear elastic problems.

Linear elastic fracture mechanics problems using the local mesh free method are performed through the singularity subtraction technique (SST), which regularizes the elastic field, before the numerical solution, thus introducing the stress intensity factors (SIF) as additional primary unknowns of the problem. This strategy result in a direct computation of the SIF and does not require a refined discretization to obtain accurate results. The high efficiency of this model strategy can be seen in the numerical results, for simple coarse nodal distributions, without any refinement around crack tips. Therefore, the reliability and robustness can also be extend for solving fracture mechanics problems.

This chapter shows that the local mesh free method, along with optimization processes, could provide stable and accurate solutions for linear elastic and fracture mechanics problems, without most known setbacks, contributing to a mainstream use of mesh-free numerical methods in the near future. For the next research projects, the local mesh free method, with the SST implementation and optimization, will be extended for the analysis of multiple crack growth problems, nonlinear plates and dynamic problems.

References

M. Aliabadi, D. Rooke, and D. Cartwright. An improved boundary element formulation for calculating stress intensity factors: Application to aerospace structures. *J. Strain Analysis*, 22(4): 1–5, 1987.

S. Atluri and S. Shen. The meshless local petrov-galerkin (mlpg) method: A simple and less-costly alternative to the finite element and boundary element methods. *CMES: Computer Modeling in Engineering and Sciences*, 3(1):11–51, 2002.

S. Atluri and T. Zhu. A new meshless local petrov-galerkin (mlpg) approach in computational mechanics. *Computational Mechanics*, 22(2):117–127, 1998.

S. Atluri and T. Zhu. New concepts in meshless methods. *International Journal for Numerical Methods in Engineering*, 47:537–556, 2000.

S. Atluri, Z. Han, and A. Rajendran. A new implementation of the meshless finite volume method through the mlpg mixed approach. *CMES: Computer Modeling in Engineering and Sciences*, 6:491–513, 2004.

A. Bagheri, R. Ehsany, M. Mahmoodabadi, and G. Baradaran. Optimization of meshless local petrov-galerkin using genetic algorithm for 3d elasto–static problems. *International Journal of Engineering*, 24(2):143–153, 2011.

G. Baradaran and M. Mahmoodabadi. Optimal pareto parametric analysis of two dimensional steady–state heat conduction problems by mlpg method. *International Journal of Engineering*, 22(4):387–406, 2009.

P. Basu, A. Jorge, S. Badri, and J. Lin. Higher-order modeling of continua by finite-element, boundary-element, meshless, and wavelet methods. *Computers and Mathematics with Applications*, 46(1):15–33, 2003.

K. Bathe. *Finite Element Procedures*. Prentice Hall, 2014.

S. Beissel and T. Belytschko. Nodal integration of the element-free galerkin method. *Computer Methods in Applied Mechanics and Engineering*, 139(1–4):49–74, 1996.

T. Belytschko, L. Gu, and Y. Y. Lu. Fracture and crack growth by element-free galerkin methods. *Modelling and Simulation in Materials Science and Engineering*, 2(3A):519–534, 1994a.

T. Belytschko, Y. Y. Lu, and L. Gu. Element-free galerkin methods. *International Journal for Numerical Methods in Engineering*, 37(2):229–256, 1994b. ISSN 1097-0207.

T. Belytschko, Y. Guo, W. Liu, and S. Xiao. A unified stability analysis of meshless particle methods. *International Journal for Numerical Methods in Engineering*, 48(9):1359–1400, 2000.

S. Bordas, T. Rabczuk, and G. Zi. Three-dimensional crack initiation, propagation, branching and junction in non-linear materials by an extended mesh free method without asymptotic enrichment. *Engineering Fracture Mechanics*, 75(5):943–960, 2008.

J. Brahtz. Stress distribution in a reentrant corner. *Transactions of the American Society of Mechanical Engineers*, 55:31–37, 1933.

J. Caicedo and A. Portela. Cracked plate analysis with the dual boundary element method and williams eigenexpansion. *J. of Engineering Analysis with Boundary Elements*, 52:16–23, 2015.

A. Carpinteri, G. Ferro, and G. Ventura. The partition of unity quadrature in element-free crack modeling. *Journal of Computers and Structures*, 81:1783–1794, 2003.

M.-Y. Cheng and D. Prayogo. Symbiotic organisms search: A new metaheuristic optimization algorithm. *Computers & Structures*, 139(15):98–112, 2014.

M. Civelek and F. Erdogan. *Crack problems for a rectangular plate and an infinite strip*, volume 19. 1982.

R. C. Eberhart and Y. Shi. *Computational Intelligence: Concepts to Implementations*. Elsevier, 2007.

M. Ebrahimnejad, N. Fallah, and A. Khoei. Adaptive refinement in the meshless finite volume method for elasticity problems. *Computers & Mathematics with Applications*, 69(12):1420–1443, 2015.

G. Fichera. *Linear Elliptic Differential Systems and Eigenvalue Problems*. Springer, 2006.

B. Finalyson. *The Method of Weighted Residuals and Variational Principles*, volume 87. Academic Press, 1972.

M. Fleming, Y. Chu, B. Moran, and T. Belytschko. Enriched element free galerkin methods for crack tip fields. *Int. J. for Numerical Methods in Engineering*, 40:1483–504, 1997.

M. Gen and R. Cheng. *Genetic Algorithms and Engineering Optimization*. Wiley, 2000.

J. H. Holland. *Adaptation in Natural and Artificial Systems*. MIT press, 1975.

C. Hwang and A. Masud. *Multiple Objectives Decision Making Methods and Applications*. Springer, 1979.

V. Kelner and O. Leonard. Application of genetic algorithms to lubrication pump stacking design. *Journal of Computational and Applied Mathematics*, 168(1):255–265, 2004.

G. Kirchhoff. Uber das gleichgewicht und die bewegung einer unendlich diinnen elastischen stabes. *J. Reine Angew. Math.*, 56(1):285–313, 1859.

G. Liu. Mesh free methods - moving beyond the finite element method. 2003.

G. Liu and Y. Gu. A local point interpolation method for stress analysis of two-dimensional solids. *Structural Engineering and Mechanics*, 11(2):221–236, 2001.

G. Liu, L. Yan, J. Wang, and Y. Gu. Point interpolation method based on local residual formulation using radial basis functions. *Structural Engineering and Mechanics*, 14:713–732, 2002.

G. Liu, G. Zhang, Y. Wang, Z. Zhong, G. Li, and X. Han. A nodal integration technique for meshfree radial point interpolation method (ni-rpim). *International Journal of Solids and Structures*, 44(11:12):3840–3860, 2007.

W. Liu, J. Ong, and R. Uras. Finite element stabilization matrices – a unification approach. *Computer Methods in Applied Mechanics and Engineering*, 53(1):13–46, 1985.

W. Liu, S. Jun, and Y. Zhang. Reproducing kernel particle methods. *International Journal for Numerical Methods in Engineering*, 20:1081–1106, 1995.

W. Liu, Y. Chen, S. Jun, J. Chen, T. Belytschko, C. Pan, R. Uras, and C. Chang. Overview and applications of the reproducing kernel particle methods. *Archives of Computational Methods in Engineering State of the Art Reviews*, 3(1):3–80, 1996.

X. Liu, Q. Xiao, and B. Karihaloo. Xfem for direct evaluation of mixed mode stress intensity factors in homogeneous and bi-materials. *Int. J. for Numerical Methods in Engineering*, 59: 1103–1118, 2004.

J. McCall. Genetic algorithms for modelling and optimisation. *Journal of Computational and Applied Mathematics*, 184(1):205–222, 2005.

A. Moussaoui and T. Bouziane. Comparative study of the effect of the parameters of sizing data on results by the meshless methods (mlpg). *World Journal of Mechanics*, 3(1):82–87, 2013.

Y. Murakami. *Linear Elliptic Differential Systems and Eigenvalue Problems*. Pergamon Press, 1987a.

Y. Murakami. *Stress intensity factors handbook, 1st edition, vol 2*. Pergamon Press, 1987b.

B. Nayroles, G. Touzot, and P. Villon. Generalizing the finite element method: Diffuse approximation and diffuse elements. *Computational Mechanics*, 10:307–318, 1992.

N. T. Nguyen, T. Q. Bui, M. N. Nguyen, and T. T. Truong. Meshfree thermomechanical crack growth simulations with new numerical integration scheme. *Engineering Fracture Mechanics*, 235(5):107–121, 2020.

T. Oliveira and A. Portela. Weak form collocation – a local meshless method in linear elasticity. *Engineering Analysis with Boundary Elements*, 73(1):144–160, 2016.

A. Portela and M. Aliabadi. Crack growth analysis using boundary elements – software. 1993.

L. Qingbo, X. Nengxiong, W. Weifeng, and L. Yazhe. Modeling of shear crack propagation in rock masses using mesh-free lrpim. *Advances in Civil Engineering*, 2021(1):1–13, 2021.

T. Rabczuk and T. Belytschko. A three-dimensional large deformation mesh free method for arbitrary evolving cracks. *Computer Methods in Applied Mechanics and Engineering*, 196(29–30):2777–2799, 2007.

J. Ringuest. *Multiobjective Optimization: Behavioral and Computational Considerations*. Kluwer, 1992.

Y. Sawaragi, H. Nakayama, and T. Tanino. *Theory of Multiobjective Optimization*. Academic Press, 1985.

R. Steuer. *Multiple Criteria Optimization: Theory, Computation, and Application*. Wiley, 1986.

G. Symm. Integral equation methods in potential theory, ii. *Proceedings of Royal Society*, A275: 33–46, 1963.

H. Tada. *The stress analysis of cracks handbook*. ASME Press, 2000.

P. Wen and M. Aliabadi. Applications of meshless method to fracture mechanics with enriched radial basis functions. *Durability of Structures and Health Monitoring*, 3:107–119, 2007.

M. Williams. Stress singularities resulting from various boundary conditions in angular corners of plates in extension. *Journal of Applied Mechanics*, pages 526–528, 1952.

L. Xanthis, M. Bernal, and C. Atkinson. The treatment of the singularities in the calculation of stress intensity factors using the integral equation method. *Comp. Meth. in Applied Mechanics Engineering*, 26:285–304, 1981.

T. Zhu, J. Zhang, and S. Atluri. A local boundary integral equation (lbie) method in computational mechanics and a meshless discretization approach. *Computational Mechanics*, 21:223–235, 1998.

O. Zienkiewicz and R. Taylor. *Finite Element and Approximation*. John Wiley & Sons, 1983.